Clim. Past Discuss., 9, 525–582, 2013
www.clim-past-discuss.net/9/525/2013/
doi:10.5194/cpd-9-525-2013

Climate of the Past Discussions

Albedo and heat transport in 3-dimensional model simulations of the early Archean climate

H. Kienert, G. Feulner, and V. Petoukhov

Potsdam Institute for Climate Impact Research, Telegrafenberg A62,
14473 Potsdam, Germany

Received: 21 December 2012 – Accepted: 16 January 2013 – Published: 24 January 2013

Correspondence to: H. Kienert (kienert@pik-potsdam.de)

Published by Copernicus Publications on behalf of the European Geosciences Union.

Abstract

At the beginning of the Archean eon (ca. 3.8 billion yr ago), the Earth's climate state was significantly different from today due to the lower solar luminosity, smaller continental fraction, higher rotation rate and, presumably, significantly larger greenhouse gas concentrations. All these aspects play a role in solutions to the "faint young Sun problem" which must explain why the ocean surface was not fully frozen at that time. Here, we present 3-dimensional model simulations of climate states that are consistent with early Archean boundary conditions and have different CO_2 concentrations, aiming at an understanding of the fundamental characteristics of the early Archean climate system. We focus on three states: one of them is ice-free, one has the same mean surface air temperature of 288 K as today's Earth and the third one is the coldest stable state in which there is still an area with liquid surface water (i.e. the critical state at the transition to a "snowball Earth"). We find a reduction in meridional heat transport compared to today which leads to a steeper latitudinal temperature profile and has atmospheric as well as oceanic contributions. Ocean surface velocities are largely zonal, and the strength of the atmospheric meridional circulation is significantly reduced in all three states. These aspects contribute to the observed relation between global mean temperature and albedo, which we suggest as a parameterisation of the ice-albedo feedback for 1-dimensional model simulations of the early Archean and thus the faint young Sun problem.

1 Introduction

During the Archean eon (3.8 billion yr to 2.5 billion yr ago), the Sun's luminosity increased from about 75 % to about 82 % of its present-day value (Bahcall et al., 2001). In this light, indicators of liquid surface water (Lowe, 1980; Walker, 1982) raise the question which mechanisms have counteracted this lower luminosity, a problem that

CPD
9, 525–582, 2013

was first explicitly phrased by Sagan and Mullen (1972) and is known as the "faint young Sun problem" (Feulner, 2012).

Most solutions that have been suggested involve larger greenhouse gas concentrations. Their warming impacts on global temperature and thus glaciation have mainly been studied with 1-dimensional radiative-convective models (e.g. Kasting et al., 1984; Kiehl and Dickinson, 1987; von Paris et al., 2008). However, these models do not represent any 3-dimensional effects as meridional heat transport or albedo changes due to continents, sea ice or clouds (Kasting, 2010). A few early studies of the Archean climate (Jenkins, 1993, 1996) have applied 3-dimensional models but were highly simplified (e.g. without a full ocean model).

This is the second in a series of papers investigating the Archean climate with 3-dimensional model simulations using a fully coupled ocean-atmosphere-sea ice model. In the first paper, we have shown that the 3-dimensional effects mentioned above significantly raise the critical CO_2 concentrations required to prevent the Earth from freezing with respect to 1-dimensional model results (Kienert et al., 2012). Here, we use the same model with identical parameters to study key characteristics of the early Archean climate, in particular the albedo and the heat transport.

On the most fundamental level, the Earth's global energy balance is set by solar irradiance and planetary albedo. Contributions to albedo variations especially arise from clouds and changes in surface type. Due to the high reflectivity of snow and ice, the sea-ice albedo feedback plays an important role in case of significant glaciation as has already been shown four decades ago by Budyko (1969). There are times in Earth's history, for which strong indications for extensive sea-ice cover or even for the occurrence of a fully frozen ocean surface in a so called "snowball state" (Kirschvink, 1992) have been found. In this context, the question of critical greenhouse gas amounts with respect to global glaciation has, e.g., already been posed and studied for the Marinoan Earth (about 650 Myr ago). In contrast to research on the Archean climate, several palaeostudies on that time period use 3-dimensional models (e.g. Voigt and

CPD
9, 525–582, 2013

Marotzke, 2010; Voigt et al., 2011) and thus include the albedo effect of changing sea-ice cover.

Meridional heat transport from low to high latitudes is effecting the latitudinal temperature profile and is thus coupled to the formation of sea ice. Therefore, the specific horizontal redistribution of heat in the climate system indirectly affects the global energy balance. In order to characterize this heat transport and the underlying atmospheric and oceanic dynamics, not only a 3-dimensional model with appropriate external boundary conditions (as, e.g. solar irradiance and differences in the Earth's rotation rate) is needed; but a realistic topography must be implemented. In the early Archean, the emerged surface area was much smaller than today (Flament, 2009) so that similarities in the dynamics of the climate system with aquaplanet (an idealised planet fully covered by oceans) states are expected. Many atmospheric modelling studies exist which assume oceanic boundary conditions without continents. But the number of aquaplanet (or near-aquaplanet) studies taking into account the coupled ocean-atmosphere system and thus the full impact of the vanishing continental fraction is very limited (Smith et al., 2006; Marshall et al., 2007; Enderton and Marshall, 2009; Ferreira et al., 2010), and none of them employs Archean boundary conditions.

Here, we show how the early Archean must have differed from the present-day climate, especially with respect to its energy balance which determines the critical greenhouse gas concentrations. Therefore, we put a special focus on albedo and heat transport when analysing the simulated climate state. We will first, in Sect. 2, describe the model as well as the modifications that were applied in order to make it applicable for the early Archean climate. We will continue in Sect. 3 with describing the key characteristics of the early Archean climate states with a special focus on albedo and heat transport which are essential for setting up a relation between greenhouse gases and global mean temperature. Before we finally use a larger set of simulations in Sect. 5 in order to suggest a parameterisation of the ice-albedo effect in the early Archean for 1-dimensional radiative-convective models, uncertainties due to our restricted knowledge

CPD
9, 525–582, 2013

of the topography and of radiative transfer in CO_2-rich atmospheres are considered in Sect. 4.

2 Model description

2.1 Original model and main settings

The simulations of the Archean climate are performed with a modified version of CLIMBER-3α (Montoya et al., 2005), which is an earth system model of intermediate complexity (EMIC, Claussen et al., 2002). CLIMBER-3α basically consists of an improved version of the ocean general circulation model MOM3 (Pacanowski and Griffies, 1999; Hofmann and Morales Maqueda, 2006), the statistical-dynamical atmosphere model POTSDAM-2 (Petoukhov et al., 2000) and the thermodynamic-dynamic sea-ice model ISIS (Fichefet and Morales Maqueda, 1997). Under pre-industrial conditions, the model reacts to a doubling of the atmospheric CO_2 concentration with a rise in surface air temperature by 3.2 K. For simulations of the last millennium and future climate, the model is well established and has contributed to different model intercomparisons (e.g. Gregory et al., 2005; Stouffer et al., 2006; Jansen et al., 2007; Plattner et al., 2008; Eby et al., 2012). In total, the model simulates approximately 200 model-years per day of integration on a single CPU, which makes it possible to perform a large number of ensemble simulations until they approach equilibrium after 5000 yr in this study. This is particularly important for investigations of deep-time palaeoclimate problems because uncertainties in boundary conditions can be systematically explored.

The ocean and sea-ice components have a horizontal resolution of 3.75°. The ocean module has 20 vertical levels with the bathymetry that we use for the simulation of the Archean ocean, and it applies a non-linear explicit free surface scheme. Vertical mixing is parameterised via the KPP scheme in the boundary layer (Large et al., 1994). As background values, we use $10\,cm^2\,s^{-1}$ for viscosity and a Bryan-Lewis profile (Bryan and Lewis, 1979) for diffusivity. The parameters for the latter are modified so that the

CPD
9, 525–582, 2013

vertical background diffusivity takes values between the same (present-day CLIMBER-3α) limits of 0.3 $cm^2 s^{-1}$ at the surface and 1.3 $cm^2 s^{-1}$ at the maximum ocean depth also for our modified topography.

The viscosity for Laplacian horizontal mixing of momentum is constant in time and depth and has a latitude-dependent cosine-profile with a maximum value of 3.2×10^9 $cm^2 s^{-1}$. Isoneutral tracer mixing is achieved via a small angle approximated (Gent and McWilliams, 1990) Redi diffusion tensor (Redi, 1982) and Gent-McWilliams parameterisation of eddy stirring (Gent and McWilliams, 1990). The respective diffusivities are constant and have values of 2.0×10^7 $cm^2 s^{-1}$ for Redi diffusion and 0.25×10^7 $cm^2 s^{-1}$ for the Gent-McWilliams parameterisation.

The atmosphere model has a resolution of 7.5° × 22.5° and assumes a linear decrease of temperature in the troposphere with a lapse rate calculated by the model as well as an isothermal stratosphere above. Instead of explicitly resolving synoptic scale processes, their statistical behaviour is modelled. In contrast to the standard version of CLIMBER-3α, we do not use the wind-anomaly model here, but keep winds fully free to evolve. The cloud scheme differentiates between stratus and cumulus clouds, with the cloud fractions depending on humidity and vertical velocity (Petoukhov et al., 2000).

Note that the land surface is free of vegetation in all our simulations of the early Archean. The following clear-sky albedo values are used: 0.17 for bare land (Tsvetsinskaya et al., 2002), as well as 0.53 and 0.72 for thick sea ice under melting and freezing conditions, respectively (Shine and Henderson-Sellers, 1985). Sea ice covered by thick snow has an albedo of 0.8 (Shine and Henderson-Sellers, 1985).

2.2 Modifications

In order to simulate the climate of the Archean, the boundary conditions which differ from today's world have to be taken into account. This includes a different bathymetry and land fraction as well as a higher rotation rate of the Earth, larger greenhouse-gas (GHG) partial-pressures (in terms of CO_2 equivalents) and a lower solar constant.

CPD
9, 525–582, 2013

2.2.1 Topography

It has long been generally accepted that 70 % or more of today's continental crust had already been separated from the mantle by the end of the Archean (Kröner, 1985). However, there is a lot of controversy and uncertainty with respect to the question of when and how fast continental crust grew. Isotopic data (e.g. Belousova et al., 2010; Dhuime et al., 2012) and theoretical arguments on the growth and subduction processes (Flament, 2009) give some indications. Several models based on the age distribution of preserved minerals or sediments (Hurley and Rand, 1969; Taylor and McLennan, 1985) suggest only a few percent of today's continental volume for the early Archean. Note however, that a study by Campbell (2003) indicates that already more than 40 % of today's crust were formed 3.8 Ga ago. The smaller fraction of emerged land has had an impact on the surface albedo of the Earth and potentially evaporation together with cloud formation; and the different bathymetry in general influences meridional heat transport with consequences on the sea-ice fraction and thus the total energy balance.

Due to the lack of knowledge regarding land distribution, there is neither a specific topography field nor a known distribution of emerged continents that could be used for model simulations. We thus use a set of fields whose details are created randomly, but which are based on a physically motivated area-per-depth distribution. Our reference topography used in this study is displayed in Fig. 1.

The area-per-depth distribution is based on a geological modelling study by Flament et al. (2008) assuming a 200 K hotter mantle as well as 20 % continental crust compared to today's value. The latter is the smallest value of their range of 20 % to 80 % for the period between 4 Ga and 2.5 Ga. For the mode of mantle cooling and thus the age distribution of the oceanic lithosphere, we have chosen the model by Labrosse and Jaupart (2007) (named LJ07 in Flament et al., 2008). As it is the medium value out of the suggested range, we have picked a maximum age of the ocean floor of 142 Ma. As can be seen in Fig. 3 in Flament et al. (2008), the resulting emerged surface area

CPD
9, 525–582, 2013

under the assumption of present day maximum orography height turns out to be about 3 % of the Earth's surface. Estimating the dynamically supported maximum elevation to be 3600 m as suggested by Rey and Coltice (2008) for the Neoarchean leads to an actually emerged surface area of about 1 %. Our random reference topography follows the resulting depth distribution of submerged continental crust, continental slope and oceanic lithosphere which is shown in Fig. 2.

In order to ensure that our results do not significantly depend on the choice of the reference topography, we have performed simulations with two additional random topographies that are also characterised by 1 % emerged surface, two topographies whose continents are distributed as archipelagos (once near the equator, once in a polar location) and three topographies with 5 % emerged surface. In Sect. 4.1, we describe the overall differences to the reference case.

2.2.2 Long wave radiative transfer

The long wave radiative (LWR) transfer code of CLIMBER-3α is based on a two-stream-approximation using integrated transmission functions (ITFs) for water vapour and CO_2 (Petoukhov et al., 2003). Latest results suggest that the most commonly used parameterisation in radiative transfer codes overestimates warming for CO_2-rich atmospheres (Wordsworth et al., 2010) due to a misrepresentation of continuum absorption. Therefore, we have tuned the model code to approximate the results of the MTCKD parameterisation (Halevy et al., 2009) in addition to implementing a dependency on total pressure motivated by the large range of CO_2 partial pressures used in our set of simulations. A single parameter (a) has been varied in our model while surface temperature and lapse rate were fixed to the values given in Halevy et al. (2009), and the outgoing longwave radiation (OLR) in our model has been compared with the results of the MTCKD parameterisation (Clough et al., 2005; Halevy et al., 2009). This comparison is shown in Fig. 3 with respect to a range of CO_2 partial pressures in a dry atmosphere and a range of relative humidity in an atmosphere with a CO_2 partial pressure of 0.5 bar. It leads to the choice of a = 0.008, with the mean deviations from the MTCKD

CPD
9, 525–582, 2013

parameterisation being about $-1.6\,\mathrm{W\,m^{-2}}$ for the dry atmosphere and about $3.1\,\mathrm{W\,m^{-2}}$ for moist atmospheres with $p\mathrm{CO_2} = 0.5$ bar.

Although the MTCKD parameterisation can arguably be considered the best representation of radiative transfer in CO_2-rich atmospheres, all three parameterisations are used in the literature and fit the observations for low-CO_2 atmospheres. Therefore, we performed additional sets of simulations of the early Archean climate in which our LWR parameter takes the values $a = 0.006$ and $a = 0.010$ in order to explore this uncertainty, and the main results from this exercise are presented in Sect. 4.2.

2.2.3 Parameterisation of atmospheric meridional cell strength

In the standard version of the model, the atmospheric meridional circulation consists of Hadley, Ferrel and polar cell in each hemisphere. When simulating the present-day climate, the cell boundary positions are in a first step fixed to latitudes of 0°, 30° and 60°, while the actual position at each point of time is in a second step adjusted according to the position of the thermal equator (Petoukhov et al., 2000). The strength of each cell is parameterised in terms of the mean temperature T_i within the cell and the temperature contrast ΔT_i between its boundaries (ϕ_{i-1} and ϕ_i):

$$|v_1(\phi)| = C_i \times 3.5 \times 10^{-2} \times \left(\frac{T_i}{T_\star}\right)^3 \times |\Delta T_i| \times \sin\left(\pi \frac{\phi - \phi_i}{\phi_{i-1} - \phi_i}\right), \quad (1)$$

where $T_\star = 273\,\mathrm{K}$, and $v_1(\phi)$ is the meridional velocity in the planetary boundary layer (in $\mathrm{m\,s^{-1}}$) and thus a measure for the cell strength (Petoukhov et al., 2000). The six coefficients C_i are originally determined empirically for the present-day climate.

In today's climate, the continent structure and orography have a significant impact on the C_i-factors due to variations of friction as can be seen, e.g., from the fact that they are not hemispherically symmetric. Since our early Archean reference topography exhibits only a very small continental fraction, we adjust these parameters to aquaplanet conditions. The temperature and velocities fields from aquaplanet simulations

CPD
9, 525–582, 2013

with a more complex atmospheric model (Marshall et al., 2007) are used to calculate values for the C_i-factors that are – after symmetrisation – appropriate for an (almost) continent-free world (Table 1). Their symmetry as well as their similarity with the present-day values give confidence in the model parameterisation.

2.2.4 Rotation rate of the Earth

The rotation rate of the Earth was higher by a factor of 1.6 in the early Archean compared to today (Zahnle and Walker, 1987) and since then, the day length has become longer due to tidal friction. While the Coriolis force explicitly enters the fundamental equations in the ocean and sea-ice module as well as in parts of the atmospheric module, it further affects the positions of the atmospheric meridional cell boundaries, potentially the number of cells, as well as the lapse rate which are the most important non-fundamental quantities in the model.

Williams (1988) presents results of a study with a general circulation model that explicitly calculates the atmospheric cell boundaries for a wide range of parameter changes, including a doubling of the Earth's rotation rate. From his results for a moist and for a dry atmosphere (for single and double present-day rotation rate), one may estimate approximate cell boundaries of 20° and 50° for a rotation rate increased by a factor of 1.6. This finding for the change in the Hadley cell boundary is supported by theoretical arguments, i.e. by the following relation for the Hadley cell boundary θ (Held and Hou, 1980):

$$\theta \leq \arctan\left(\left[(1+2R)^{1/2}-1\right]^{1/2}\right),$$
$$R = \frac{gH\Delta T}{(\Omega a)^2}. \quad (2)$$

Equation (2) gives a value of $\theta = 30^\circ$ for present-day input parameters (Navarra and Boccaletti, 2002), and $\Omega = 1.6$ leads to $\theta \leq 20.6^\circ$. In order to keep the mean cell

CPD
9, 525–582, 2013

boundaries at the grid cell boundaries of the model, we change them to 22.5° and 52.5° which are multiples of our model resolution of 7.5° in latitude.

The lapse rate in CLIMBER-3α is dependent on the local temperature T_a, specific humidity q_s and cumulus cloud fraction n_c (Petoukhov et al., 2000):

$$\Gamma = \Gamma_0 + \Gamma_1 \times (T_a - 273.16\,\mathrm{K}) \times (1 - a_q \times q_s^2) - \Gamma_2 \times n_c, \quad (3)$$

where Γ_0, Γ_1, Γ_2 and a_q are model parameters. The dependency of the lapse rate on the Earth's rotation rate enters via the coefficients Γ_i which are fixed in the standard model version and are more generally proportional to $k_0(\Omega)^{-1}$ (Zilitinkevich, 1970), with $k_0(\Omega)$ given as follows:

$$k_0 = 1 + \left(\frac{\Omega}{\Omega_{PD}}\right)^{0.25} \times (c_{vd}/c_{pd}), \quad (4)$$

where Ω_{PD} is the present-day rotation rate, and c_{vd} and c_{pd} are the constant volume and constant pressure heat capacities of the present-day atmosphere. For a rotation rate of $\Omega = 1.6$, the values of the parameters are $\Gamma_0 = 5.1 \times 10^{-3}$, $\Gamma_1 = 6.1 \times 10^{-5}$, $\Gamma_2 = 9.0 \times 10^{-4}$ and $a_q = 1171$.

2.2.5 Solar constant, orbital parameters and atmospheric composition

As this study focuses on the early Archean, the solar constant in the model has been reduced by 25 % to 1024 $\mathrm{W\,m^{-2}}$ (cf. Sect. 1). The orbital parameters of the Earth are fixed to the values of the year 1950 (Berger, 1978). Regarding atmospheric composition, we apply different CO_2 partial pressures in addition to a nitrogen (N_2) partial pressure of 0.8 bar as described in Sect. 3. Rayleigh scattering has been adjusted to respect changes in the CO_2 concentration (Pierrehumbert, 2010), and the impact of differences in total atmospheric pressure is taken into account in the longwave radiation module as well as indirectly in the calculation of the tropopause height.

CPD
9, 525–582, 2013

2.3 Overall impact of technical modifications

In order to be able to implement some of the above adjustments to early Archean boundary conditions, some preparatory code modifications had to be applied which also had an impact on the simulated present-day state. Firstly, the coefficients Γ_i in the lapse rate calculation are now explicitly calculated instead of being fixed, so that slightly different values arise also for present-day conditions. Secondly, the parameter a in the longwave radiation scheme has been changed. We further had to extend the range of latitudes in which filtering of fast modes had to be applied for reasons of numeric stability. Additionally, more appropriate sea-ice albedo values have been chosen. Finally, the wind stress has been set free.

As the model is validated for the pre-industrial climate (present-day continents, vegetation and ice sheets, $S_0 = 1365\,\mathrm{W\,m^{-2}}$, $p\mathrm{CO_2} = 280\,\mathrm{ppm}$), these changes shall only have a minor effect on the overall climate state. Figure 4 shows the impact of these technical changes on the pre-industrial latitudinal SAT profile. Global mean overall warming due to these changes is 1.8 K which is smaller than the differences between present-day climate states simulated with 12 EMICs in a recent intercomparison project (Eby et al., 2012).

3 Characteristics of three early Archean climate states

As found in Kienert et al. (2012) with the same model and under the same boundary conditions, a CO_2 partial pressure of 0.40 bar is required to prevent the Earth's ocean surface from fully freezing at the beginning of the Archean. Furthermore, a partial pressure of 0.6 bar is sufficient to keep the Earth at a temperature close to the present-day mean SAT of 288 K. These CO_2 amounts are significantly higher than previously estimated with 1-dimensional models (Kasting et al., 1984; Kiehl and Dickinson, 1987; von Paris et al., 2008). In addition, the difference in CO_2 partial pressure between the states is very small (factor of 1.5 between the critical state and the state with 288 K) which

CPD
9, 525–582, 2013

is mainly caused by the ice albedo feedback that is neglected in the 1-dimensional model studies. In the following, we will examine the characteristics of these two states as well as of an ice-free state (0.8 bar, 300 K mean SAT), and compare them to the pre-industrial climate.

The surface air temperature field results from an interplay of the insolation distribution, the 2-dimensional albedo field and the greenhouse effect, with further modification due to the heat transport processes in the ocean and in the atmosphere. The latitudinal profile of the surface air temperatures is shown in Fig. 5. Note the strong cooling influence of sea ice in the polar regions for the colder climate states.

In the following, we will have a more detailed look at the effects which determine the SAT profile.

3.1 Surface and planetary albedo

At first order, the global energy balance of the Earth in different climate states is determined by the albedo and its latitudinal changes. Figure 6 shows the latitudinal distribution of annual mean surface as well as total planetary albedo for all four states. The two main reasons for variations in albedo are differences in sea-ice cover (with impact on the surface and planetary albedo) and changes in cloud cover (directly impacting only the planetary albedo). Clouds are a considerable source of uncertainty in model simulations (Stephens, 2005; Cesana and Chepfer, 2012) but can have a significant impact on the energy balance of the Archean Earth (Goldblatt and Zahnle, 2011). At the same time, simulations of the sea-ice albedo feedback are more reliable. Furthermore, the significantly smaller continental fraction in the early Archean implies a reduction of surface albedo in snow-free regions compared to climate states with present-day topography. These factors will be discussed in more detail in the following.

CPD
9, 525–582, 2013

3.1.1 Surface albedo and sea-ice cover

As the Earth in our simulations of the early Archean is covered almost completely with water, its surface albedo profile in Fig. 6 is very steep near the ice-boundary. Remarkably, the ice line for the early Archean 288 K state is very similar to the Southern Hemisphere ice boundary in the present-day climate which is caused by the presence of the Antarctic continent. The reason for the early Archean state being as warm as the present-day state even though such a low annual mean ice-line is also present in the Northern Hemisphere lies in the higher equatorial temperatures. We further observe that the sea ice is almost completely covered by snow, even for the critical state which exhibits a low sea-ice boundary of 34° (defined by 10 % annual mean sea-ice cover). This results in a high overall surface albedo of 0.37 for the critical state in contrast to 0.12 for today's climate state and thus a substantial global cooling.

In order to judge the impact of the topography on surface albedo, two comparisons are instructive: First of all, a state with fixed present-day surface types and topography but without sea ice ($S = 0.75 \times S_0$, $pCO_2 = 0.8$ bar, $\Omega = 1.0$) has a mean surface albedo of 0.11 compared to only 0.07 for our ice-free early Archean topography. And secondly, the early Archean surface albedo in the always ice-free equatorial region (between 34° N and 34° S) is reduced from 0.09 to 0.07 compared to the present-day topography (numbers based on the two states with mean SAT of 288 K) which is a relatively small difference. The overall impact of our early Archean topography on the surface albedo is therefore comparably small.

3.1.2 Critical sea-ice latitude

The sea-ice boundary, and thus approximately the mean surface albedo, corresponding to a specific global mean surface temperature is determined by the latitudinal structure of radiation and heat transport. The stability of a critical state with a sea-ice boundary near the equator is, e.g., supported by comparatively high equatorial temperatures. Since the higher rotation rate of the early Archean indeed increases the equator-to-pole

CPD
9, 525–582, 2013

temperature difference compared to present-day rotation rate (cf. Kienert et al., 2012), this is a relevant contribution towards a critical sea-ice boundary at a lower latitude. However, competing effects play a role in the early Archean climate and promote a higher critical sea-ice latitude: Firstly, the small land-fraction leads to a reduced surface albedo at ice-free latitudes, thus especially around the equator (see above). And secondly, the greenhouse radiative forcing which compensates for the 25 % reduction in solar luminosity has a relatively uniform latitudinal distribution instead of a strong equatorial maximum like the insolation. All these boundary conditions are specific to the early Archean climate and contribute to the critical sea-ice boundary to 34° in our simulations.

To study the relative contributions of topography and rotation rate, we have performed simulations in which these boundary conditions were changed separately (cf. Table 2). Only adjusting the topography to the early Archean would lead to a critical sea-ice boundary of 47° which is, as expected, clearly higher than the 34° for the additionally faster rotating Earth. In simulations with present-day topography, we find overall lower critical sea-ice latitudes. But it is confirmed that a relatively low rotation rate of $\Omega = 1.0$ leads to a higher critical sea-ice latitude, namely 38°, than a high rotation rate of $\Omega = 1.6$, namely 30°.

Note that the critical sea-ice latitude (and thus the albedo of the critical state) also depends on how sea ice is treated in the model. In general, it has been observed that runaway glaciation is more difficult (or even impossible) in models which employ a low sea-ice and/or snow albedo or neglect sea-ice dynamics. One palaeoclimate problem for which these effects have been studied are “snowball Earth” glaciations during the Neoproterozoic. The sea-ice boundary for a soft snowball Earth state (continental glaciation at the equator) was found to be 25° in an atmospheric GCM with a mixed layer ocean (bare sea-ice albedo between 0.6 and 0.7; Hyde et al., 2000). This value approximately corresponds to results of a more complex, fully coupled general circulation model amounting to about 27° for Marinoan as well as present-day continental boundary conditions (Voigt et al., 2011; Voigt and Marotzke, 2010). In contrast to this,

CPD
9, 525–582, 2013

simulations with the CAM model (Collins et al., 2004) find a stable sea-ice boundary even lower than 12° if a small sea-ice albedo of 0.45 is applied (Pierrehumbert et al., 2011). Similarly high sea-ice fractions (critical sea-ice latitudes between 5–15°) were also found by Abbot et al. (2011) for stable so called *Jormungand states* with the CAM atmosphere model coupled to an ocean mixed layer that neglects ocean heat transport and sea-ice dynamics and uses a large difference between bare sea-ice albedo (0.45) and snow covered sea-ice albedo (0.79). However, it has been shown that such narrow waterbelt states become unstable when sea-ice dynamics are taken into account (Lewis et al., 2007; Voigt and Abbot, 2012). Nevertheless, the spread of results among different studies due to specific model properties and sea-ice settings is significant and also simulations with complex models support the possibility of stable glaciation up to 10° in the Neoproterozoic (Yang et al., 2012a).

Note that the possibility of such stable states with a narrow belt of open water in the Neoproterozoic does not necessarily imply the existence of such states during the Archean where the reduction in solar luminosity results in a relative decrease of energy input around the equator even when compensated by enhanced levels of greenhouse gases. Furthermore, our model uses both a low value of the bare sea-ice albedo in agreement with observations of different types of sea ice (as, e.g., reviewed by Warren et al., 2002) and takes sea-ice dynamics into account. Thus, we consider the lack of a stable waterbelt state in our simulations robust. A dedicated study of the sensitivity of our critical sea-ice latitude under early Archean boundary conditions with respect to sea-ice properties will be presented in a future paper.

3.1.3 Planetary albedo and clouds

The planetary albedo is more complicated than the surface albedo due to the contributions of clouds. Clouds, however, play an important role not only by means of changes to the planetary albedo and the direct warming due to the absorption of longwave radiation, but also indirectly by modifying the LWR spectrum and thus influencing the greenhouse effect of different gases: Goldblatt and Zahnle (2011) find that the greenhouse

CPD
9, 525–582, 2013

effect of CO_2 is overestimated by 20 to 25 % in model simulations of the Archean climate that completely neglect clouds (for pCO_2 between 0.01 bar and 0.1 bar).

In general, there is a significant spread in the results of state-of-the-art models when simulating cloud cover, and differences to satellite observations are quite large (Cesana and Chepfer, 2012). In Fig. 7, the total pre-industrial and present-day cloud fractions simulated with our model are compared to results from other models as well as observations. We find that our results are within the range of those from climate models which took part in the CMIP5 intercomparison project (dashed lines, data from the pre-industrial control simulations, Taylor et al., 2012). In low- and mid-latitudes, the annual mean cloudiness simulated with our model is closer to observations (CALIPSO-GOCCP data v2.1, Chepfer et al., 2010) than most of the other models, but there is a tendency to overestimate the cloud fraction in the cold polar regions above ice.

Our model distinguishes stratus and cumulus clouds and their latitudinal profiles are shown in Fig. 8. Differences in cloud fraction between the states are strongest in the tropics. There, but not restricted to this area, colder temperatures lead to a larger stratus cloud and a lower cumulus cloud fraction and vice versa. The differences in stratus clouds turn out to be much larger than the differences in cumulus clouds so that they dominate the results for the total cloudiness.

The stratus cloud fraction in our model has an explicit $r^{1.5}$ dependency on relative humidity r which decreases for an unchanged water mass if temperature and thus saturation humidity increase. This is consistent with results by Yang et al. (2012b), who find overall smaller fractions of low-level clouds (between the surface and the level of 700 hPa) for warmer states.

In contrast to this, the cumulus cloud fraction does not fundamentally depend on relative humidity but is instead determined by a combination of effective vertical velocity and specific humidity. The latter must reduce in case of lower temperatures due to the smaller saturation humidity, thus explaining the changes in cumulus cloud fraction described above.

CPD
9, 525–582, 2013

The latitudinal distribution of clouds is in total strongly influenced by the atmospheric cell boundaries, as can be seen in Fig. 8 from the minima in cloud fraction that have shifted from 30° to 22.5° in concordance with the high pressure area at the boundaries between the Hadley and Ferrel cells. This shift reflects the higher rotation rate of the Earth in the early Archean and takes place near the sea-ice boundary of the critical state, a region in which the local energy balance is especially important in determining the critical CO_2 partial pressure and the maximum stable sea-ice extent.

These differences in clouds between the present-day state and the three early Archean states have an impact on the planetary albedo as well as on the long wave radiation. It is therefore desirable to quantify their impact on Earth's energy balance. Of course, the radiative forcing (e.g. Hansen et al., 2005; Forster et al., 2007) due to clouds as well as their impact on surface temperature strongly depends on the different properties of the climate states, so that we can only point out which radiative contribution the simulated clouds give to our three early Archean reference states compared to the impact which clouds have under pre-industrial boundary conditions.

In a set of experiments, we have instantaneously removed all clouds in different equilibrium states. The resulting total net radiative imbalance at the top of the atmosphere (TOA) is plotted against global mean temperature in Fig. 9, and the results for the first nine years are linearly extrapolated to zero temperature change in order to receive the initial radiative forcing. We thus in principle follow the method by Gregory et al. (2004). The radiative imbalance is positive in all cases, which implies that the clouds were cooling the climate system and that their removal leads to warming. However, in the absence of clouds, less longwave radiation is absorbed by the atmosphere so that it first cools even though the surface absorbs additional shortwave radiation. Therefore, it is not possible to deduce the initial radiative forcing from extrapolation to zero surface air temperature. Thus, in contrast to Gregory et al. (2004), we instead base our analysis on surface temperature. This is justified because we find a linear relationship for the first simulated years (Fig. 9).

CPD
9, 525–582, 2013

Under pre-industrial conditions, the radiative forcing corresponding to a removal of the clouds is 28.8 $W m^{-2}$ (black line). This is in stark contrast to 17.2 $W m^{-2}$ in case of a climate state with a solar insolation reduced to 75 %, pCO_2 = 0.48 bar and present-day topography which has a similar global mean SAT of 288 K (green dashed line). The difference is obviously caused by the fact that the main impact of the clouds is an increase of planetary albedo which has a larger effect in terms of radiative forcing if the solar insolation is higher. With respect to the three states of the early Archean, we observe that the radiative effect resulting from a removal of the clouds is smaller for colder states (9.3 $W m^{-2}$, 17.5 $W m^{-2}$ and 23.0 $W m^{-2}$ for the three states with pCO_2 of 0.4 bar, 0.6 bar and 0.8 bar). This is the case even though there are more clouds in the colder states, and it can be explained by the fact that the impact of clouds on the total, planetary albedo gets reduced if there is already a high albedo due to the presence of sea ice.

We can conclude that the clouds simulated with our model provide a net cooling of the climate system and that differences in the strength of this effect between our four reference states (pre-industrial and early Archean) are dominantly caused by differences in solar radiation and sea-ice amount. These differences in cloud radiative forcing are much larger than those between climate states that have a similar temperature or sea-ice fraction (illustrated by the use of identical colour in Fig. 9) but differ with respect to rotation rate and continental fraction (solid lines for early Archean and dashed lines for present-day boundary conditions): 9.3 $W m^{-2}$ vs. 10.2 $W m^{-2}$ for the critical states, and 17.5 $W m^{-2}$ vs. 17.2 $W m^{-2}$ for the states with a mean SAT of 288 K.

As the contributions of cumulus clouds to the total radiative forcing are very small, ranging between 1 % and 9 %, we do not analyse the differences between simulated cumulus and stratus clouds in detail.

Note that these radiative forcing values alone cannot be directly related to the equilibrium temperature changes finally resulting from the removal of clouds because feedback mechanisms as the ice-albedo effect act on longer timescales and differ between the states (cf. Fig. 9). Furthermore, the vertical resolution of the cloud module or

CPD
9, 525–582, 2013

changes in cloud properties which are not taken into account in our model (as, e.g., the droplet size) may have an impact on the radiative forcing. In this context, general constraints for the maximum cloud contribution to Archean warming are provided by Goldblatt and Zahnle (2011) who also review such processes which might strongly modify Archean cloud fractions and which are not represented in our model. For example, the size of cloud particles depends on the abundance of cloud condensation nuclei which are partly biogenic; and it was suggested that their absence in the Archean may have been responsible for significant warming (Rosing et al., 2010).

3.2 Lapse rate

A further substantial impact on surface air temperature is provided by changes in the lapse rate. For fixed effective radiative temperature and effective radiative height, a lower lapse rate implies a lower surface air temperature. In our model, the 2-dimensional lapse rate field explicitly depends on temperature and humidity. The lapse rate is therefore coupled to changes in, e.g., sea-ice formation while it is (sometimes only in the lower levels) kept fixed at the adiabatic values in many studies with 1-dimensional models (e.g. Kasting et al., 1984; Goldblatt et al., 2009). Figure 10 shows the differences in lapse rate between the three simulated early Archean climate states and the pre-industrial state which already includes our modifications regarding lapse rate calculation (cf. Sect. 2.2.4) and compares well with observational data (Stone and Carlson, 1979). From Eq. (3), we see that the lapse rate increases with increasing temperature and decreases with rising humiditiy. Figure 10 shows the significantly lower lapse rate of the colder states in high latitudes, which is consistent with a positive temperature feedback. We observed that the situation is different in the warmer, equatorial regions where the negative feedback due to the water vapour term dominates: warmer states with more water vapour show a lower lapse rate, thus decreasing surface air temperature.

As the lapse rate regionally differs by up to about $2\,\mathrm{K\,km^{-1}}$, the impact on surface air temperatures is up to around 20 K with an effective radiative height of about 10 km.

CPD
9, 525–582, 2013

Due to the opposite effects in equatorial and polar regions, the lapse rate changes contribute to a further steepening of the temperature profile in the course of a cooling climate. This facilitates sea-ice formation in the higher latitudes and thus acts towards increasing the critical CO_2 partial pressure while it at the same time stabilises low latitude sea-ice boundaries.

3.3 Atmospheric dynamics

Large scale atmospheric and oceanic dynamics are amongst the most important characteristics of the climate system. They play a significant role in setting up horizontal heat transport and thus interact with the radiative balance in determining the planet's temperature field.

The dynamic state of the atmosphere is given by the meridional circulation cells, the zonal winds as well as the azonal component. In our model, the mean cell boundaries are prescribed (cf. Sect. 2.2.3), but their seasonal fluctuations as well as their strengths depend on the temperature field. Figure 11 shows annual mean maxima of the stream functions, thus illustrating the cell boundaries located closer to the equator, the symmetry between the two hemispheres and the changes in strength. All states of the early Archean have lower cell strengths than the pre-industrial reference case. The cell strengths are the combined effect of a different temperature field in the absence of larger continents and the modified cell strength parameters (Table 1). The latter have been chosen such that they provide the cell strengths from Marshall et al. (2007) when their aquaplanet temperature field is applied; and the maxima of the stream functions for the partially glaciated state are not too different from the results by Marshall et al. (2007) even though the temperature field is determined not only by the aquaplanet conditions but also by the other changes to early Archean boundary conditions.

The warmer Archean states show a smaller strength because the reduction in the temperature difference between the cell boundaries has a dominant effect over the general warming (cf. the proportionality to $T_i^3 \times \Delta T$ in Eq. 1). Though under different boundary conditions, this temperature dependency of the Hadley cell strengths

CPD
9, 525–582, 2013

is qualitatively confirmed by a set of experiments with varying solar irradiance by Yang et al. (2012a).

The maxima of the annual-mean zonal winds are shown in Fig. 12. They are consistently shifted equatorwards and the relative order of strengths reflects the meridional cell strengths which set the pressure and wind-stress fields. With respect to these wind speeds, the simulation applying $pCO_2 = 0.6$ bar is most similar to the aquaplanet simulation by Marshall et al. (2007) which assumes present-day CO_2 and solar forcing and exhibits a sea-ice boundary of 55°. The azonal component of the wind is not explicitly depicted here, but it is implicitly taken into account in the atmospheric heat transport discussed in Sect. 3.5.

3.4 Ocean dynamics

Due to the almost negligible land fraction, the ocean circulation was entirely different in the early Archean compared to today. Under present-day topography, the overturning circulation as well as horizontal currents contribute to heat transport and are thus important for the planet's energy balance.

In the absence of significant land masses, the meridional overturning circulation mainly consists of symmetric cells (Fig. 13). In contrast to today's thermohaline circulation, they mirror the atmospheric cells in the early Archean because of the wind stress acting as the driver. This circulation is expected to show strong similarities with aquaplanet simulations because of the small land fraction, while differences and asymmetries may of course arise due to the non-uniform random ocean depth as well as the differences in further boundary conditions. The aquaplanet simulations by Marshall et al. (2007) under present-day radiative forcing indeed show a shallow, wind-driven oceanic overturning circulation with the location of the cells corresponding to the atmosphere as in our simulations of the Archean. In their as well as in our simulations, the majority of the transport by the strong circulation cells adjacent to the equator is located in the upper 600 m. The transport of these cells (maxima of annual mean stream function) turns out to be 81 Sv ($pCO_2 = 0.4$ bar), 99 Sv ($pCO_2 = 0.6$ bar)

CPD
9, 525–582, 2013

and 71 Sv (pCO_2 = 0.8 bar) and is therefore in all three early Archean simulations larger than in Marshall et al. (2007) under present-day forcing (about 60 Sv). Furthermore, the transport below the top grid cell of the model (25 m deep) is mostly in the opposite direction of the relatively strong surface currents and reaches deeper when the currents are stronger. While the meridional surface velocities without Gent-McWilliams (GM) component are larger when the state is colder (corresponding to the order of wind velocities), the total transport is affected by the poleward GM velocities which are largest in the 288 K state.

The surface velocities have a very characteristic structure under present-day topography, e.g. producing the large and strong subtropical gyres. However, in case of very small land fraction they closely resemble a purely zonal flow (Fig. 14). For the early Archean topography, the strength of the surface velocities (Fig. 15) is correlated with the strength of the atmospheric meridional cells. The surface velocities for the state with a CO_2 partial pressure of 0.6 bar reach about 0.25 m s^{-1} at the equator and about 0.16 m s^{-1} in mid-latitudes. This is in contrast to the values of 0.8 m s^{-1} and 0.2 m s^{-1} found by Marshall et al. (2007) which are not only overall higher but also show a high factor of 4 between currents corresponding to the easterly trade winds and mid-latitude westerlies.

3.5 Heat transport

The atmospheric and oceanic dynamics described above result in a meridional heat transport that is significant in determining the sea-ice boundary and thus the full global energy balance. Figure 16 shows the total heat transport as well as the oceanic and atmospheric contributions. Depending on the latitude, the oceanic contribution to the difference in heat transport between the pre-industrial and the early Archean climate (with 288 K SAT) is of a similar magnitude as the atmospheric contribution, which shows the relevance of using a full ocean model. In general, there is a reduction of atmospheric and of oceanic heat transport when going from the present-day state to the early Archean state with the similar global mean SAT and pCO_2 = 0.6 bar. In the

CPD
9, 525–582, 2013

ocean, this is expected because of the reduction of the meridional overturning circulation due to the absence of continental boundaries. In the atmosphere, a reduction of advective heat transport in the tropics is found as well as a reduction of synoptic heat transport in the mid-latitudes of a similar magnitude. The increase of heat transport (in ice-free latitudes) with decreasing temperature and growing sea ice is consistent with the behaviour of ocean and atmosphere dynamics in Figs. 11 and 13.

The peak in total heat transport is not shifted by more than one model grid cell and is at either 33.75° or 37.5° in the pre-industrial simulation as well as in all three Archean simulations. Thus, the classic results of 35° by Stone (1978) is also valid for our early Archean states.

4 Impact of uncertainties in topography and radiative transfer

As described in Sect. 2, the largely unknown topography and the difficulties involved in determining long-wave radiative transfer in CO_2-rich atmospheres constitute some uncertainty. The results presented in Sect. 3 are based on a specific reference topography and fixed parameters for the LWR scheme, and here we investigate the impact that different choices would have.

4.1 Topographies

In order to understand the impact of topography, we do still focus on the two states with $pCO_2 = 0.60$ bar and $pCO_2 = 0.80$ bar as in the analysis above. But as the critical state with $pCO_2 = 0.40$ bar is close to instability with respect to complete glaciation, we substitute it in this section by a state with $pCO_2 = 0.45$ bar.

Figure 17 shows the latitudinal SAT profiles for the different topographies and for each of the three CO_2 partial pressures. Three of the topographies are exemplarily depicted in Fig. 18.

CPD
9, 525–582, 2013

The temperature differences among the various topographies are minor for the simulations with $pCO_2 = 0.45$ bar and $pCO_2 = 0.80$ bar which implies that the sea-ice boundary is similar. We therefore find neither a significant dependence of the critical CO_2 partial pressure nor of the state characteristics described in Sect. 3 on the topographies.

The situation is somewhat different for the simulation with $pCO_2 = 0.60$ bar. Here, we find a much wider temperature spread as well as significant hemispheric asymmetries in some of the simulations. The latter are strongest in the topography *D* with 1 % emerged surface which is ice-free in the Northern Hemisphere but has a mean sea-ice boundary of 49° in the Southern Hemisphere. Already the ice-free case with a CO_2 partial pressure of 0.8 bar shows higher temperatures at the North Pole than at the South Pole; and for an overall colder climate in case of $pCO_2 = 0.6$ bar, this effect is enhanced by the ice-albedo feedback. The higher temperature in the Northern Hemisphere goes along with a higher northward heat transport compared to the other topographies, which again is due to a significantly larger northward ocean heat transport (caused by the specific ocean bottom topography) which is not fully compensated by the weaker atmospheric transport.

In contrast to the impact of the ocean bottom topography on heat transport, the surface albedo difference appears to be negligible. For the ice-free state, we find global mean surface albedo values of 0.073–0.074 for the topographies with 1 % emerged surface (including the two archipelagos), and 0.077–0.078 for those with 5 % emerged surface depending on the latitudes of the continents. Indeed, the mean SAT of the five states with lower albedo is slightly higher than that of the states with higher albedo (299.8 K vs. 299.7 K). But the difference is smaller than the spread among topographies of the same type, and we already see from Fig. 17 that those states with the slightly higher surface albedo are not necessarily warmer than those with a lower albedo value.

We can thus conclude that the impact on the results due to differences between our early Archean topographies is minor for the critical and ice-free states, but can result in asymmetries between the two hemispheres for partially ice-covered states because of changes in oceanic heat transport depending on bottom topography.

CPD
9, 525–582, 2013

4.2 LWR parameterisation

Further uncertainty in the climate simulations of the early Archean necessarily arises because the absorption of long-wave radiation in CO_2-rich atmospheres is not exactly known. As described in Sect. 2.2.2, we have tuned the appropriate parameter a of our LWR-module to approximate the MTCKD-parameterisation (Clough et al., 2005; Halevy et al., 2009) ($a = 0.008$) but checked the impact of different choices in additional sets of simulations.

In Kienert et al. (2012), it was already noted that the critical CO_2 partial pressure is reduced from 0.40 bar to 0.28 bar when changing $a = 0.008$ to $a = 0.010$, which is still about five times higher than critical partial pressures in studies with 1-dimensional models (e.g. von Paris et al., 2008). The partial pressures needed to provide a mean SAT of 288 K and to provide an ice-free state are 0.4 bar and 0.55 bar, respectively. If we reduce the LWR parameter to a value of $a = 0.006$ (cf. Fig. 3) in order to estimate the magnitude of the involved uncertainty and thus approximate the approach by Meadows and Crisp (1996) (cf. CA parameterisation in Halevy et al., 2009), we find a critical CO_2 partial pressure of 0.65 bar. In that case, a partial pressure of 0.9 bar is required for a mean SAT similar to today and $pCO_2 = 1.2$ bar to inhibit the formation of sea ice.

Even though it has been argued that previous simulations with 1-dimensional models that used a parameterisation which is approximated by $a = 0.010$ overestimated CO_2-induced greenhouse warming (Wordsworth et al., 2010), the differences in temperature resulting from different parameter choices call for more detailed research on the radiative effect of CO_2-rich palaeoatmospheres, in particular for laboratory experiments investigating the continuum absorption for conditions appropriate for early Earth.

5 Ice-albedo parameterisation for 1-dimensional models of the early Archean

Earlier simulations of the climate of the Archean Earth have mainly relied on 1-dimensional radiative-convective models. As these models allow for an efficient

CPD
9, 525–582, 2013

investigation of the radiative impact of more complex greenhouse gas mixtures and for studying atmospheric chemistry, they will certainly continue to play a role in research on the faint young Sun problem. Their largest shortcoming in determining the critical CO_2 concentration required to prevent the Earth from freezing lies in the omission of the ice-albedo feedback (Kienert et al., 2012).

For climate states not too different from today, Wang and Stone (1980) have suggested to use a parameterisation of the albedo in terms of global mean temperature in these types of models. However, their relation is not expected to be valid for the early Archean because of the differences in surface type and meridional heat transport compared to today (cf. Sect. 3). Here, we suggest to use the relation between global mean SAT and surface or planetary albedo from our model simulations as a more appropriate parameterisation. This also implies that no ad-hoc assumption on the global mean SAT of the critical state is necessary anymore.

The relations found in our 3-dimensional simulations (Fig. 19) exhibit an approximately linear behaviour and suggest the following approximations, where $\overline{T}$ is the global mean SAT in Kelvin:

$$A_S = \begin{cases} 0.81, & \text{for } \overline{T} < 268 \\ 0.37 - 0.01 \times (\overline{T} - 268), & \text{for } 268 \leq \overline{T} \leq 298 \\ 0.07, & \text{for } \overline{T} > 298 \end{cases} \quad (5)$$

$$A_P = \begin{cases} 0.74, & \text{for } \overline{T} < 268 \\ 0.41 - 0.004 \times (\overline{T} - 268), & \text{for } 268 \leq \overline{T} \leq 298 \end{cases} \quad (6)$$

Both observed relations turn out to be not well represented by linear approximations in case of present-day rotation rate and are clearly non-linear for present-day continental topography. Therefore, one cannot expect this linearity to be a fundamental property. If one applies the Stefan Boltzmann law to the global mean planetary albedo

CPD
9, 525–582, 2013

(A_P) and global mean effective temperature (T_{eff}),

$$\sigma T_{eff}^4 = \frac{1}{4} S_0 (1 - A_P), \quad (7)$$

the relation is not far from linear in the relevant temperature range, but changes in lapse rate and effective radiative height may introduce non-linearity. From a different perspective, one can argue from an approximation of the temperature and surface-albedo dependency on the sea-ice boundary (cf. Wang and Stone, 1980) that a purely geometric relation of sea-ice boundary and surface albedo without presence of land (as is almost the case for the early Archean) allows for a more linear behaviour in Fig. 19.

For comparison, we show the surface-albedo parameterisation by Wang and Stone (1980) for the large range of global mean SAT between 250 K and 305 K in panel (a) of Fig. 19 (dashed blue line, assuming our snow and ocean albedo values). The difference between this parameterisation and the surface albedo in our simulations is significant which underlines the advantage of using the relation based on our modelling results as a parameterisation.

6 Conclusions

We have modified a three-dimensional climate model in order to simulate possible climate states of the early Archean that have different CO_2 partial pressures: 0.4 bar (critical state, 268 K global mean SAT), 0.6 bar (288 K state) and 0.8 bar (ice-free, 300 K global mean SAT). Key characteristics of the climate states contributing to the global energy balance have been presented. Some Archean boundary conditions as the Earth's rotation rate and solar insolation are well known, but the continental fraction and distribution, for example, involve significant uncertainty or are even unknown. Therefore, we have based our study on one random reference continent distribution, but presented the results of additional simulations in order to estimate the uncertainty due to the topography, thus making use of the computational efficiency of our model.

CPD
9, 525–582, 2013

The effect of changes in continent distribution or an increase of the continental fraction from about 1 to 5 % turn out to be minor. As the long-wave radiative properties of CO_2-rich atmospheres are still under debate, we have further shown the impact of different parameterisations in this respect, which result in significantly different CO_2 partial pressures of the critical states.

Regarding the overall latitudinal SAT profiles of the simulated climate states, it was found that the one corresponding to the state with 288 K is quite symmetric and exhibits a larger equator-to-pole difference than in the pre-industrial climate. As the sea-ice albedo feedback plays a significant role in setting this temperature profile and the required CO_2 partial pressure, we have presented the sea-ice boundaries corresponding to the different states and found that basically all sea ice is snow-covered which leads to a high mean surface albedo. The radiative impact of clouds in our simulations is largely due to stratus clouds which in total provide a cooling effect, and the corresponding radiative forcing is smaller than today in all three early Archean states due to the lower solar luminosity.

The atmospheric meridional circulation as well as zonal winds are weaker in the early Archean state with 288 K mean SAT compared to present-day. This contributes to the overall reduction of meridional heat transport found for the early Archean, with the strongest reduction occurring for the warmest (ice-free) early Archean state. The second contribution to it comes from the oceanic heat transport which is decreased going along with the lack of a deep and far-reaching meridional overturning circulation in the absence of significant continental boundaries. Apart from the shallow wind-driven overturning cells, the main oceanic circulation pattern consists of zonal flows.

Furthermore, based on the relation between surface (or planetary) albedo and surface air temperature, we suggest a parameterisation of the ice-albedo effect for 1-dimensional radiative-convective models. Modelling studies of the faint young Sun problem have so far not taken this effect into account, and an ensemble of three-dimensional simulations over a broad range of greenhouse gas forcing has been

CPD
9, 525–582, 2013

required for providing a suitable parameterisation which can be used in future studies with simpler models.

Acknowledgements. We are grateful to David Ferreira for providing electronic data as well as Anthony Bosse, Sylvain Bouillon, Dim Coumou, Alexey Eliseev, Nicolas Flament, Matthias Hofmann, Miguel Morales Maqueda and Stefan Petri for discussions. We acknowledge the World Climate Research Programme's Working Group on Coupled Modelling, which is responsible for CMIP, and we thank the climate modelling groups for producing and making available their model output. We also thank the involved groups/institutions for making available the CALIPSO-GOCCP cloud data. HK acknowledges support by the Evangelisches Studienwerk Villigst e.V.

References

Abbot, D. S., Voigt, A., and Koll, D.: The Jormungand global climate state and implications for Neoproterozoic glaciations, J. Geophys. Res., 116, D18103, doi:10.1029/2011JD015927, 2011. 540

Bahcall, J. N., Pinsonneault, M. H., and Basu, S.: Solar models: current epoch and time dependences, neutrinos, and helioseismological properties, Astrophys. J., 555, 990–1012, doi:10.1086/321493, 2001. 526

Belousova, E. A., Kostitsyn, Y. A., Griffin, W. L., Begg, G. C., O'Reilly, S. Y., and Pearson, N. J.: The growth of the continental crust: constraints from zircon Hf-isotope data, Lithos, 119, 457–466, doi:10.1016/j.lithos.2010.07.024, 2010. 531

Berger, A. L.: Long-term variations of daily insolation and quaternary climatic changes., J. Atmos. Sci., 35, 2362–2367, doi:10.1175/1520-0469(1978)035<2362:LTVODI>2.0.CO;2, 1978. 535

Bryan, K. and Lewis, L. J.: A water mass model of the world ocean, J. Geophys. Res., 84, 2503–2517, doi:10.1029/JC084iC05p02503, 1979. 529

Budyko, M. I.: The effect of solar radiation variations on the climate of the earth, Tellus, 21, 611–619, doi:10.1111/j.2153-3490.1969.tb00466.x, 1969. 527

Campbell, I. H.: Constraints on continental growth models from Nb/U ratios in the 3.5 Ga Barberton and other Archaean basalt-komatiite suites, Am. J. Sci., 303, 319–351, doi:10.2475/ajs.303.4.319, 2003. 531

CPD
9, 525–582, 2013

Cesana, G. and Chepfer, H.: How well do climate models simulate cloud vertical structure? A comparison between CALIPSO-GOCCP satellite observations and CMIP5 models, Geophys. Res. Lett., 39, L20803, doi:10.1029/2012GL053153, 2012. 537, 541

Chepfer, H., Bony, S., Winker, D., Cesana, G., Dufresne, J. L., Minnis, P., Stubenrauch, C. J., and Zeng, S.: The GCM-Oriented CALIPSO Cloud Product (CALIPSO-GOCCP), J. Geophys. Res.-Atmos., 115, D00H16, doi:10.1029/2009JD012251, 2010. 541, 570

Claussen, M., Mysak, L. A., Weaver, A. J., Crucifix, M., Fichefet, T., Loutre, M.-F., Weber, S. L., Alcamo, J., Alexeev, V. A., Berger, A., Calov, R., Ganopolski, A., Goosse, H., Lohmann, G., Lunkeit, F., Mokhov, I. I., Petoukhov, V., Stone, P., and Wang, Z.: Earth system models of intermediate complexity: closing the gap in the spectrum of climate system models, Clim. Dynam., 18, 579–586, doi:10.1007/s00382-001-0200-1, 2002. 529

Clough, S. A., Shephard, M. W., Mlawer, E. J., Delamere, J. S., Iacono, M. J., Cady-Pereira, K., Boukabara, S., and Brown, P. D.: Atmospheric radiative transfer modeling: a summary of the AER codes, J. Quant. Spectrosc. Radiat. Transfer, 91, 233–244, 2005. 532, 550

Collins, W. D., Rasch, P. J., Boville, B. A., Hack, J. J., McCaa, J. R., Williamson, D. L., Kiehl, J. T., Briegleb, B., Bitz, C., and Lin, S. J.: Description of the NCAR community atmosphere model (CAM 3.0), Technical Note TN-464+ STR, National Center for Atmospheric Research, Boulder, CO, 2004. 540

Dhuime, B., Hawkesworth, C. J., Cawood, P. A., and Storey, C. D.: A change in the geodynamics of continental growth 3 billion years ago, Science, 335, 1334–1336, doi:10.1126/science.1216066, 2012. 531

Eby, M., Weaver, A. J., Alexander, K., Zickfeld, K., Abe-Ouchi, A., Cimatoribus, A. A., Crespin, E., Drijfhout, S. S., Edwards, N. R., Eliseev, A. V., Feulner, G., Fichefet, T., Forest, C. E., Goosse, H., Holden, P. B., Joos, F., Kawamiya, M., Kicklighter, D., Kienert, H., Matsumoto, K., Mokhov, I. I., Monier, E., Olsen, S. M., Pedersen, J. O. P., Perrette, M., Philippon-Berthier, G., Ridgwell, A., Schlosser, A., Schneider von Deimling, T., Shaffer, G., Smith, R. S., Spahni, R., Sokolov, A. P., Steinacher, M., Tachiiri, K., Tokos, K., Yoshimori, M., Zeng, N., and Zhao, F.: Historical and idealized climate model experiments: an EMIC intercomparison, Clim. Past Discuss., 8, 4121–4181, doi:10.5194/cpd-8-4121-2012, 2012. 529, 536

Enderton, D. and Marshall, J.: Explorations of atmosphere-ocean-ice climates on an aquaplanet and their meridional energy transports, J. Atm. Sci., 66, 1593–1611, doi:10.1175/2008JAS2680.1, 2009. 528

CPD
9, 525–582, 2013

Ferreira, D., Marshall, J., and Campin, J. M.: Localization of deep water formation: role of atmospheric moisture transport and geometrical constraints on ocean circulation, J. Climatol., 23, 1456–1476, doi:10.1175/2009JCLI3197.1, 2010. 528
Feulner, G.: The faint young Sun problem, Rev. Geophys., 50, RG2006, doi:10.1029/2011RG000375, 2012. 527
Fichefet, T. and Morales Maqueda, M. A.: Sensitivity of a global sea ice model to the treatment of ice thermodynamics and dynamics, J. Geophys. Res.-Oceans, 102, 12609–12646, 1997. 529
Flament, N.: Secular cooling of the solid Earth, emergence of the continents, and evolution of Earth's external envelopes, Ph.D. thesis, University of Sydney and École Normale Supérieure de Lyon, 2009. 528, 531
Flament, N., Coltice, N., and Rey, P. F.: A case for late-Archaean continental emergence from thermal evolution models and hypsometry, Earth Planet. Sci. Lett., 275, 326–336, doi:10.1016/j.epsl.2008.08.029, 2008. 531
Forster, P., Ramaswamy, V., Artaxo, P., Berntsen, T., Betts, R., Fahey, D. W., Haywood, J., Lean, J., Lowe, D. C., Myhre, G., Nganga, J., Prinn, R., Raga, G., Schulz, M., and Van Dorland, R.: Climate Change 2007: The Physical Science Basis. Contribution of Working Group I to the Fourth Assessment Report of the Intergovernmental Panel on Climate Change, chap. Changes in Atmospheric Constituents and in Radiative Forcing, Cambridge University Press, Cambridge, United Kingdom and New York, NY, USA, 2007. 542
Gent, P. R. and McWilliams, J. C.: Isopycnal mixing in ocean circulation models, J. Phys. Oceanogr., 20, 150–155, doi:10.1175/1520-0485(1990)020<0150:IMIOCM>2.0.CO;2, 1990. 530
Goldblatt, C. and Zahnle, K. J.: Clouds and the faint young Sun paradox, Clim. Past, 7, 203–220, doi:10.5194/cp-7-203-2011, 2011.537, 540, 544
Goldblatt, C., Claire, M. W., Lenton, T. M., Matthews, A. J., Watson, A. J., and Zahnle, K. J.: Nitrogen-enhanced greenhouse warming on early Earth, Nat. Geosci., 2, 891–896, doi:10.1038/ngeo692, 2009. 544
Gregory, J. M., Ingram, W. J., Palmer, M. A., Jones, G. S., Stott, P. A., Thorpe, R. B., Lowe, J. A., Johns, T. C., and Williams, K. D.: A new method for diagnosing radiative forcing and climate sensitivity, Geophys. Res. Lett., 31, L03205, doi:10.1029/2003GL018747, 2004. 542
Gregory, J. M., Dixon, K. W., Stouffer, R. J., Weaver, A. J., Driesschaert, E., Eby, M., Fichefet, T., Hasumi, H., Hu, A., Jungclaus, J. H., Kamenkovich, I. V., Levermann, A., Montoya, M.,

CPD
9, 525–582, 2013

Murakami, S., Nawrath, S., Oka, A., Sokolov, A. P., and Thorpe, R. B.: A model intercomparison of changes in the Atlantic thermohaline circulation in response to increasing atmospheric CO_2 concentration, Geophys. Res. Lett., 32, L12703, doi:10.1029/2005GL023209, 2005. 529

Halevy, I., Pierrehumbert, R. T., and Schrag, D. P.: Radiative transfer in CO_2-rich paleoatmospheres, J. Geophys. Res., 114, D18112, doi:10.1029/2009JD011915, 2009. 532, 550, 566

Hansen, J., Sato, M., Ruedy, R., Nazarenko, L., Lacis, A., Schmidt, G. A., Russell, G., Aleinov, I., Bauer, M., Bauer, S., Bell, N., Cairns, B., Canuto, V., Chandler, M., Cheng, Y., Del Genio, A., Faluvegi, G., Fleming, E., Friend, A., Hall, T., Jackman, C., Kelley, M., Kiang, N., Koch, D., Lean, J., Lerner, J., Lo, K., Menon, S., Miller, R., Minnis, P., Novakov, T., Oinas, V., Perlwitz, J., Perlwitz, J., Rind, D., Romanou, A., Shindell, D., Stone, P., Sun, S., Tausnev, N., Thresher, D., Wielicki, B., Wong, T., Yao, M., and Zhang, S.: Efficacy of climate forcings, J. Geophys. Res.-Atmos., 110, D18104, doi:10.1029/2005JD005776, 2005. 542

Held, I. M. and Hou, A. Y.: Nonlinear axially symmetric circulations in a nearly inviscid atmosphere, J. Atmos. Sci., 37, 515–533, 1980. 534

Hofmann, M. and Morales Maqueda, M. A.: Performance of a second-order moments advection scheme in an ocean general circulation model, J. Geophys. Res.-Oceans, 111, C05006, doi:10.1029/2005JC003279, 2006. 529

Hurley, P. M. and Rand, J. R.: Pre-drift continental nuclei, Science, 164, 1229–1242, doi:10.1126/science.164.3885.1229, 1969. 531

Hyde, W. T., Crowley, T. J., Baum, S. K., and Peltier, W. R.: Neoproterozoic "snowball Earth" simulations with a coupled climate/ice-sheet model, Nature, 405, 425–429, doi:10.1038/35013005, 2000. 539

Jansen, E., Overpeck, J., Briffa, K. R., Duplessy, J.-C., Joos, F., Masson-Delmotte, V., Olago, D., Otto-Bliesner, B., Peltier, W. R., Rahmstorf, S., Ramesh, R., Raynaud, D., Rind, D., Solomina, O., Villalba, R., and Zhang, D.: Climate Change 2007: The Physical Science Basis. Contribution of Working Group I to the Fourth Assessment Report of the Intergovernmental Panel on Climate Change, chap. Palaeoclimate, Cambridge University Press, Cambridge, United Kingdom and New York, NY, USA, 2007. 529

Jenkins, G. S.: A general circulation model study of the effects of faster rotation rate, enhanced CO_2 concentration, and reduced solar forcing: implications for the faint young sun paradox, J. Geophys. Res., 98, 20803–20811, doi:10.1029/93JD02056, 1993. 527

CPD
9, 525–582, 2013

Jenkins, G. S.: A sensitivity study of changes in Earth's rotation rate with an atmospheric general circulation model, Global Planet. Change, 11, 141–154, doi:10.1016/0921-8181(95)00050-X, 1996. 527

Kasting, J. F.: Early Earth: faint young Sun redux, Nature, 464, 687–689, doi:10.1038/464687a, 2010. 527

Kasting, J. F., Pollack, J. B., and Crisp, D.: Effects of high CO_2 levels on surface temperature and atmospheric oxidation state of the early earth, J. Atmos. Chem., 1, 403–428, doi:10.1007/BF00053803, 1984. 527, 536, 544

Kiehl, J. T. and Dickinson, R. E.: A study of the radiative effects of enhanced atmospheric CO_2 and CH_4 on early Earth surface temperatures, J. Geophys. Res., 92, 2991–2998, doi:10.1029/JD092iD03p02991, 1987. 527, 536

Kienert, H., Feulner, G., and Petoukhov, V.: Faint young Sun problem more severe due to ice-albedo feedback and higher rotation rate of the early Earth, Geophys. Res. Lett., 39, L23710, doi:10.1029/2012GL054381, 2012. 527, 536, 539, 550, 551

Kirschvink, J. L.: Late proterozoic low-latitude global glaciation: the snowballl earth, in: The Proterozoic Biosphere: A Multidisciplinary Study, edited by: Schopf, J. W. and Klein, C., 51–52, Cambridge University Press, Cambridge, 1992. 527

Kröner, A.: Evolution of the archean continental crust, Annu. Rev. Earth Planet. Sci., 13, 49–74, doi:10.1146/annurev.ea.13.050185.000405, 1985. 531

Labrosse, S. and Jaupart, C.: Thermal evolution of the Earth: secular changes and fluctuations of plate characteristics, Earth Planet. Sci. Lett., 260, 465–481, doi:10.1016/j.epsl.2007.05.046, 2007. 531

Large, W. G., McWilliams, J. C., and Doney, S. C.: Oceanic vertical mixing: a review and a model with a nonlocal boundary layer parameterization, Rev. Geophys., 32, 363–403, doi:10.1029/94RG01872, 1994. 529

Lewis, J. P., Weaver, A. J., and Eby, M.: Snowball versus slushball Earth: dynamic versus nondynamic sea ice?, J. Geophys. Res.-Oceans, 112, doi:10.1029/2006JC004037, 2007. 540

Lowe, D. R.: Archean sedimentation, Annu. Rev. Earth Planet. Sci., 8, 145–167, doi:10.1146/annurev.ea.08.050180.001045, 1980. 526

Marshall, J., Ferreira, D., Campin, J.-M., and Enderton, D.: Mean climate and variability of the atmosphere and ocean on an aquaplanet, J. Atmos. Sci., 64, 4270–4286, doi:10.1175/2007JAS2226.1, 2007. 528, 534, 545, 546, 547, 562

CPD
9, 525–582, 2013

Meadows, V. S. and Crisp, D.: Ground-based near-infrared observations of the Venus nightside: the thermal structure and water abundance near the surface, J. Geophys. Res., 101, 4595–4622, 1996. 550

Montoya, M., Griesel, A., Levermann, A., Mignot, J., Hofmann, M., Ganopolski, A., and Rahmstorf, S.: The earth system model of intermediate complexity CLIMBER-3α. Part 1: description and performance for present-day conditions, Clim. Dynam., 25, 237–263, doi:10.1007/s00382-005-0044-1, 2005. 529

Navarra, A. and Boccaletti, G.: Numerical general circulation experiments of sensitivity to Earth rotation rate, Clim. Dynam., 19, 467–483, doi:10.1007/s00382-002-0238-8, 2002. 534

Pacanowski, R. C. and Griffies, S. M.: The MOM-3 manual, Tech. Rep. 4, NOAA/Geophyical Fluid Dynamics Laboratory, Princeton, NJ, USA, 1999. 529

Petoukhov, V., Ganopolski, A., Brovkin, V., Claussen, M., Eliseev, A., Kubatzki, C., and Rahmstorf, S.: CLIMBER-2: a climate system model of intermediate complexity. Part I: model description and performance for present climate, Clim. Dynam., 16, 1–17, 2000. 529, 530, 533, 535

Petoukhov, V., Ganopolski, A., and Claussen, M.: POTSDAM – a set of atmosphere statistical-dynamical models: theoretical background, Tech. Rep. 81, Potsdam Institute for Climate Impact Research, 2003. 532

Pierrehumbert, R. T.: Principles of Planetary Climate, Cambridge University Press, Cambridge, 2010. 535

Pierrehumbert, R. T., Abbot, D. S., Voigt, A., and Koll, D.: Climate of the Neoproterozoic, in: Annual Review of Earth and Planetary Sciences, edited by: Jeanloz, R. and Freeman, K. H., Vol. 39, 417–460, Annual Reviews, Palo Alto, 2011. 540

Plattner, G.-K., Knutti, R., Joos, F., Stocker, T. F., von Bloh, W., Brovkin, V., Cameron, D., Driesschaert, E., Dutkiewicz, S., Eby, M., Edwards, N. R., Fichefet, T., Hargreaves, J. C., Jones, C. D., Loutre, M. F., Matthews, H. D., Mouchet, A., Müller, S. A., Nawrath, S., Price, A., Sokolov, A., Strassmann, K. M., and Weaver, A. J.: Long-term climate commitments projected with climate carbon cycle models, J. Climatol., 21, 2721, doi:10.1175/2007JCLI1905.1, 2008. 529

Redi, M. H.: Oceanic isopycnal mixing by coordinate rotation, J. Phys. Oceanogr., 12, 1154–1158, doi:10.1175/1520-0485(1982)012<1154:OIMBCR>2.0.CO;2, 1982. 530

Rey, P. F. and Coltice, N.: Neoarchean lithospheric strengthening and the coupling of Earth's geochemical reservoirs, Geology, 36, 635–638, 2008. 532

CPD
9, 525–582, 2013

Rosing, M. T., Bird, D. K., Sleep, N. H., and Bjerrum, C. J.: No climate paradox under the faint early Sun, Nature, 464, 744–747, doi:10.1038/nature08955, 2010. 544
Sagan, C. and Mullen, G.: Earth and Mars: Evolution of atmospheres and surface temperatures, Science, 177, 52–56, doi:10.1126/science.177.4043.52, 1972. 527
Shine, K. P. and Henderson-Sellers, A.: The sensitivity of a thermodynamic sea ice model to changes in surface albedo parameterization, J. Geophys. Res., 90, 2243–2250, doi:10.1029/JD090iD01p02243, 1985. 530
Smith, R. S., Dubois, C., and Marotzke, J.: Global climate and ocean circulation on an aqua-planet ocean-atmosphere general circulation model, J. Climatol., 19, 4719–4737, 2006. 528
Stephens, G. L.: Cloud feedbacks in the climate system: a critical review, J. Climatol., 18, 237–273, doi:10.1175/JCLI-3243.1, 2005. 537
Stone, P. H.: Constraints on dynamical transports of energy on a spherical planet, Dynam. Atmos. Ocean, 2, 123–139, doi:10.1016/0377-0265(78)90006-4, 1978. 548
Stone, P. H. and Carlson, J. H.: Atmospheric lapse rate regimes and their parameterization, J. Atmos. Sci., 36, 415–423, 1979. 544
Stouffer, R. J., Yin, J., Gregory, J. M., Dixon, K. W., Spelman, M. J., Hurlin, W., Weaver, A. J., Eby, M., Flato, G. M., Hasumi, H., Hu, A., Jungclaus, J. H., Kamenkovich, I. V., Levermann, A., Montoya, M., Murakami, S., Nawrath, S., Oka, A., Peltier, W. R., Robitaille, D. Y., Sokolov, A., Vettoretti, G., and Weber, S. L.: Investigating the causes of the response of the thermohaline circulation to past and future climate changes, J. Climatol., 19, 1365–1387, doi:10.1175/JCLI3689.1, 2006. 529
Taylor, K. E., Stouffer, R. J., and Meehl, G. A.: An overview of CMIP5 and the experiment design, B. Am. Meteorol. Soc., 93, 485–498, doi:10.1175/BAMS-D-11-00094.1, 2012. 541, 570
Taylor, S. R. and McLennan, S. M.: The Continental Crust: Its Composition and Evolution, Blackwell, Palo Alto, CA, 1985. 531
Tsvetsinskaya, E. A., Schaaf, C. B., Gao, F., Strahler, A. H., Dickinson, R. E., Zeng, X., and Lucht, W.: Relating MODIS-derived surface albedo to soils and rock types over Northern Africa and the Arabian peninsula, Geophys. Res. Lett., 29, 1353 pp., doi:10.1029/2001GL014096, 2002. 530
Voigt, A. and Abbot, D. S.: Sea-ice dynamics strongly promote Snowball Earth initiation and destabilize tropical sea-ice margins, Clim. Past Discuss., 8, 2445–2475, doi:10.5194/cpd-8-2445-2012, 2012. 540

CPD
9, 525–582, 2013

Voigt, A. and Marotzke, J.: The transition from the present-day climate to a modern Snowball Earth, Clim. Dynam., 35, 887–905, doi:10.1007/s00382-009-0633-5, 2010. 527, 539
Voigt, A., Abbot, D. S., Pierrehumbert, R. T., and Marotzke, J.: Initiation of a Marinoan Snowball Earth in a state-of-the-art atmosphere-ocean general circulation model, Clim. Past, 7, 249–263, doi:10.5194/cp-7-249-2011, 2011.528, 539
von Paris, P., Rauer, H., Lee Grenfell, J., Patzer, B., Hedelt, P., Stracke, B., Trautmann, T., and Schreier, F.: Warming the early earth – CO_2 reconsidered, Planet. Space Sci., 56, 1244–1259, doi:10.1016/j.pss.2008.04.008, 2008. 527, 536, 550
Walker, J. C. G.: Climatic factors on the Archean Earth, Palaeogeogr. Palaeocl., 40, 1–11, doi:10.1016/0031-0182(82)90082-7, 1982. 526
Wang, W. C. and Stone, P. H.: Effect of ice-albedo feedback on global sensitivity in a one-dimensional radiative-convective climate model, J. Atmos. Sci., 37, 545–552, doi:10.1175/1520-0469(1980)037<0545:EOIAFO>2.0.CO;2, 1980. 551, 552, 582
Warren, S. G., Brandt, R. E., Grenfell, T. C., and McKay, C. P.: Snowball Earth: ice thickness on the tropical ocean, J. Geophys. Res.-Oceans, 107, 3167, doi:10.1029/2001JC001123, 2002. 540
Williams, G. P.: The dynamical range of global circulations – I, Clim. Dynam., 2, 205–260, doi:10.1007/BF01371320, 1988. 534
Wordsworth, R., Forget, F., and Eymet, V.: Infrared collision-induced and far-line absorption in dense CO_2 atmospheres, Icarus, 210, 992–997, doi:10.1016/j.icarus.2010.06.010, 2010. 532, 550
Yang, J., Peltier, W. R., and Hu, Y.: The initiation of modern "Soft Snowball" and "Hard Snowball" climates in CCSM3. Part I: the influences of solar luminosity, CO_2 concentration, and the sea ice/snow albedo parameterization, J. Climatol., 25, 2711–2736, doi:10.1175/JCLI-D-11-00189.1, 2012a. 540, 546
Yang, J., Peltier, W. R., and Hu, Y.: The initiation of modern "Soft Snowball" and "Hard Snowball" climates in CCSM3. Part II: climate dynamic feedbacks, J. Climatol., 25, 2737–2754, doi:10.1175/JCLI-D-11-00190.1, 2012b. 541
Zahnle, K. and Walker, J. C. G.: A constant daylength during the precambrian era?, Precambrian Res., 37, 95–105, doi:10.1016/0301-9268(87)90073-8, 1987. 534
Zilitinkevich, S. S.: Dynamics of the Atmospheric Boundary Layer, Gidrometeoizdat, Leningrad, 1970. 535

CPD
9, 525–582, 2013

Table 1. Empirical C_i-factors for the parameterisation of the atmospheric meridional cell strength in terms of the temperature field. Present-day values are from the standard version of CLIMBER-3α, and aquaplanet values are based on a comparison with modelling results by Marshall et al. (2007). For the Archean, we have chosen the factors in the last column which are close to the aquaplanet values, but symmetrical about the equator.

	Present-day	Aquaplanet	Archean
Northern Polar cell	0.1	0.22	0.21
Northern Ferrel cell	0.4	0.36	0.36
Northern Hadley cell	4.5	3.36	3.40
Southern Hadley cell	3.0	3.45	3.40
Southern Ferrel cell	0.8	0.36	0.36
Southern Polar cell	0.2	0.21	0.21

CPD
9, 525–582, 2013

Table 2. Critical sea-ice latitudes for simulations in which topography and rotation rate Ω were adjusted separately to early Archean (EA) boundary conditions.

	Present-day topography	EA topography
Ω = 1.0	38°	47°
Ω = 1.6	30°	34°

CPD
9, 525–582, 2013

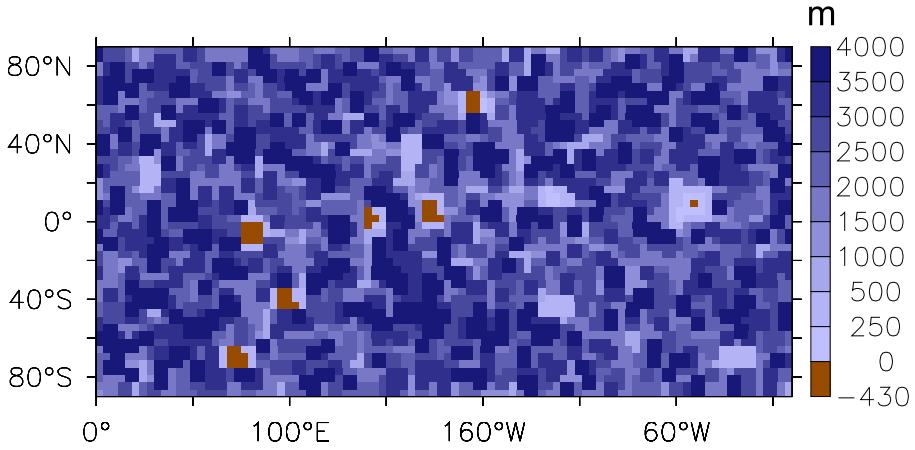

Fig. 1. Early Archean topography used in this study. This specific ocean depth field is created randomly but respects an area-per-depth distribution based on geological modelling and exhibits an emerged surface area of 1 %.

CPD
9, 525–582, 2013

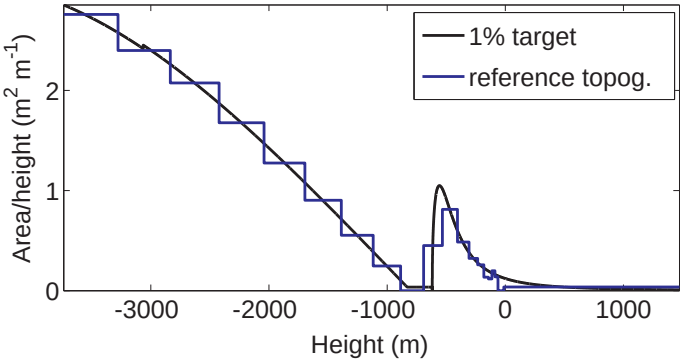

Fig. 2. Area-per-depth distribution used in the simulations of the early Archean. The black line represents the physically motivated distribution, and the blue line shows the actual distribution underlying the discrete model topography field.

CPD
9, 525–582, 2013

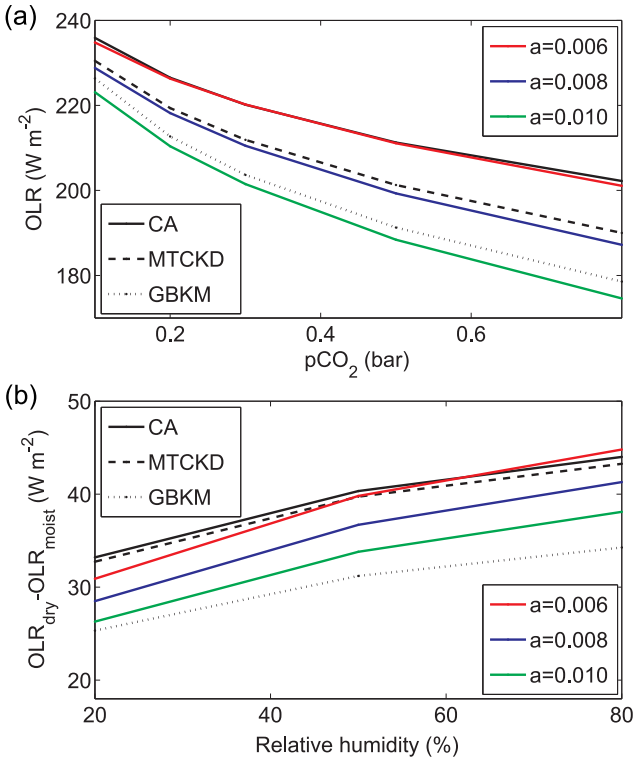

Fig. 3. Tuning of the longwave radiation scheme to approximate the MTCKD parameterisation for high partial pressures of CO_2. Black lines show the outgoing longwave radiation under fixed boundary conditions for three different parameterisations as in Halevy et al. (2009). Coloured lines show the outgoing longwave radiation under the same boundary conditions as in our model simulations for different values of the parameter *a*. Panel **(a)** displays the dependency on CO_2 partial pressure in a dry atmosphere, while panel **(b)** shows the effect of water vapour on an atmosphere with $pCO_2 = 0.5$ bar in terms of OLR. Note the different scales of the two panels.

CPD
9, 525–582, 2013

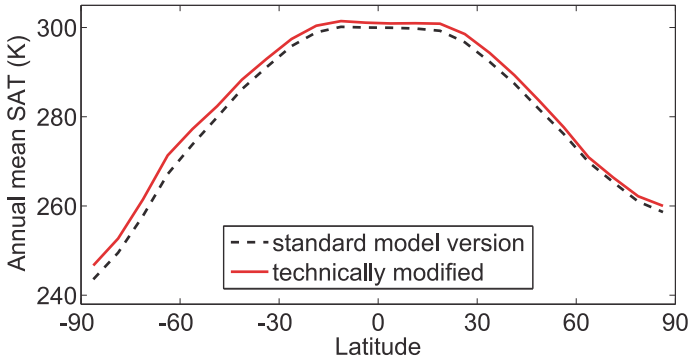

Fig. 4. Pre-industrial SAT profile for standard model equilibrium and the version with implementation of technical changes required for later on applying Archean boundary conditions.

CPD
9, 525–582, 2013

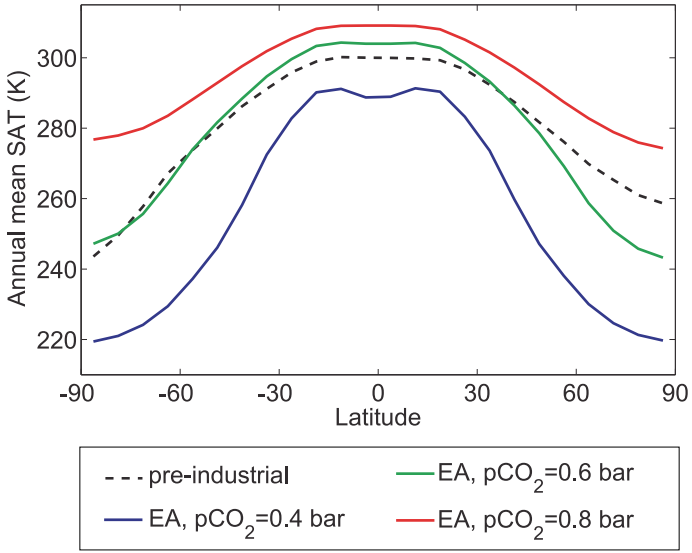

Fig. 5. Annual and zonal mean SAT for the following states: pre-industrial (black), the critical state of the early Archean ($pCO_2 = 0.4$ bar, blue), the state of the early Archean with present-day mean SAT of 288 K ($pCO_2 = 0.6$ bar, green) and an ice-free state ($pCO_2 = 0.8$ bar, red).

CPD
9, 525–582, 2013

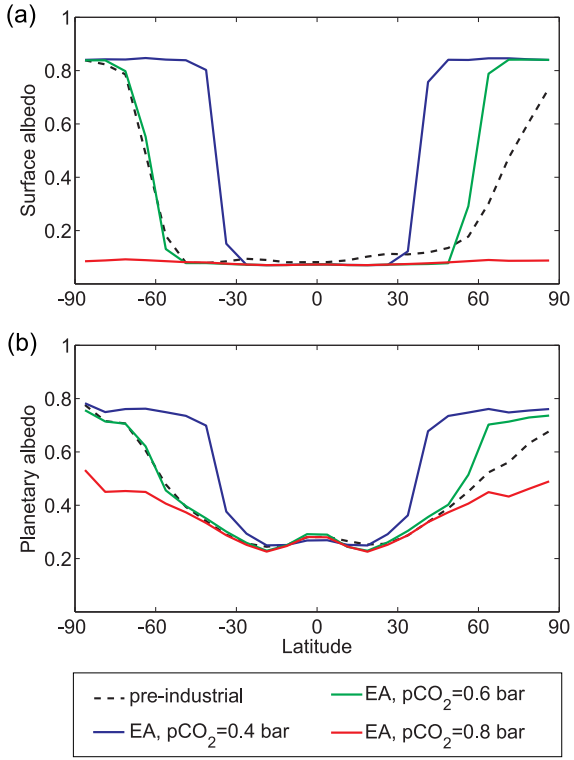

Fig. 6. Annual and zonal mean surface and planetary albedo for the following states: pre-industrial (black), the critical state of the early Archean ($pCO_2 = 0.4$ bar, blue), the state of the early Archean with present-day mean SAT of 288 K ($pCO_2 = 0.6$ bar, green) and an ice-free state ($pCO_2 = 0.8$ bar, red).

CPD
9, 525–582, 2013

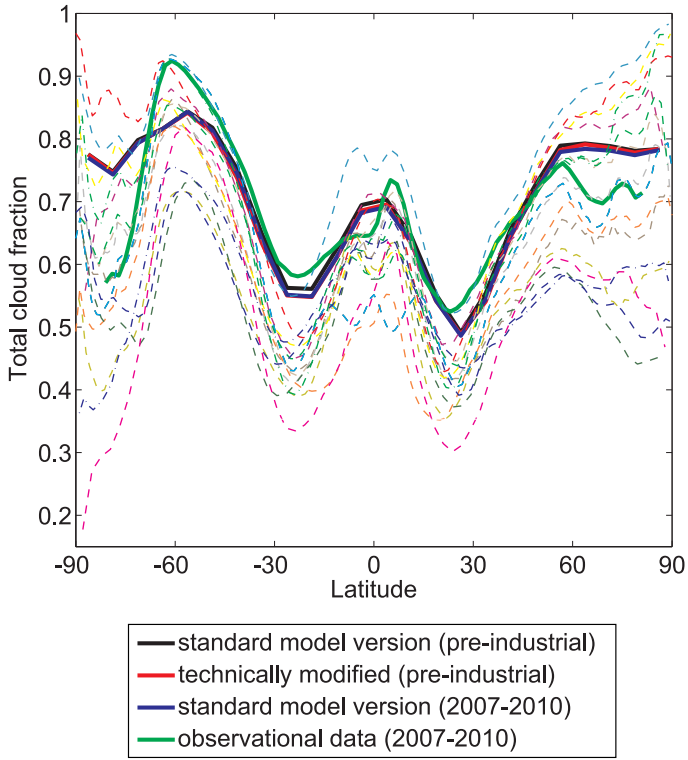

Fig. 7. Annual and zonal mean total cloud fraction. The solid lines show results from our model for the present-day (blue) and pre-industrial climate (standard model version in black, technically modified as in Sect. 2.3 given in red) as well as observational data (green, CALIPSO-GOCCP v2.1, Chepfer et al., 2010). For comparison, the dashed lines represent the results from simulations of the pre-industrial climate with different CMIP5 models (Taylor et al., 2012).

CPD
9, 525–582, 2013

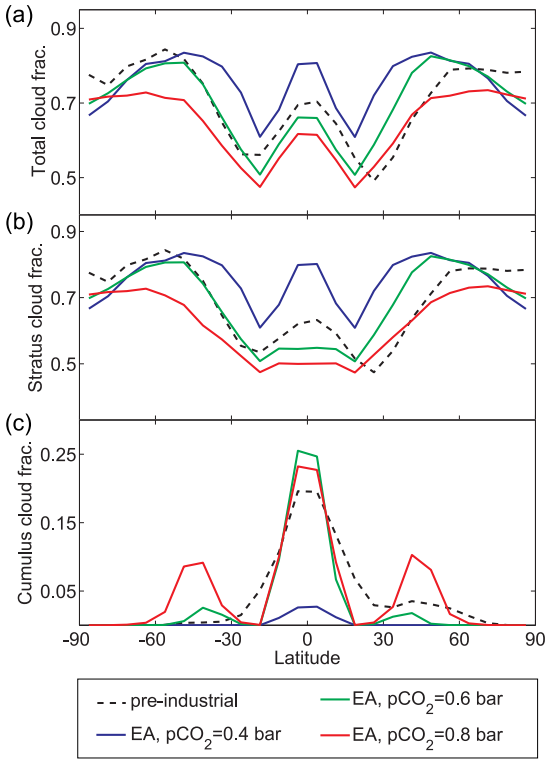

Fig. 8. Annual and zonal mean total cloud fraction in the pre-industrial climate and the three early Archean climate states: **(a)** total fraction, **(b)** stratus cloud fraction, **(c)** cumulus cloud fraction.

CPD
9, 525–582, 2013

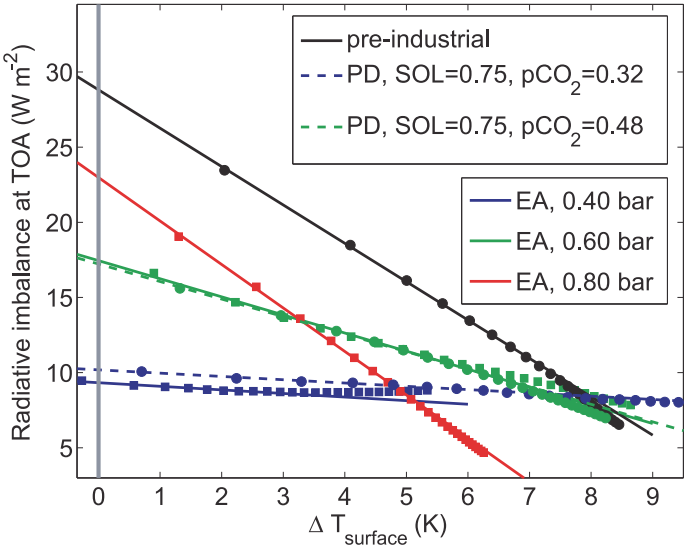

Fig. 9. Radiative imbalance at the top of the atmosphere when all clouds are removed instantaneously in different equilibrium climate states. Each point in the scatter plot corresponds to the mean value of one year. The linear fits are based on the first 9 yr in all cases. The simulation of the pre-industrial climate has been performed with the model version including the technical changes as in Sect. 2.3. Note that the x-axis represents surface and not surface air temperature.

CPD
9, 525–582, 2013

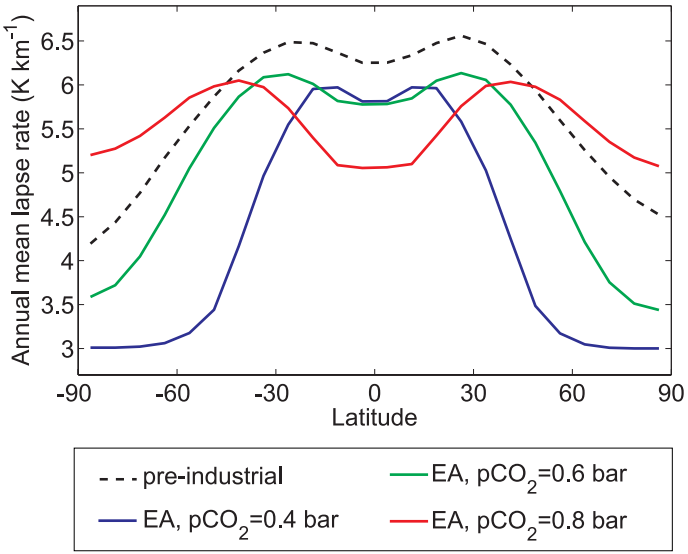

Fig. 10. Annual and zonal mean lapse rate for the following states: pre-industrial with the technical modifications from Sect. 2.2.4 (black), the critical state of the early Archean (pCO_2 = 0.4 bar, blue), the state of the early Archean with present-day mean SAT of 288 K (pCO_2 = 0.6 bar, green) and an ice-free state (pCO_2 = 0.8 bar, red).

CPD
9, 525–582, 2013

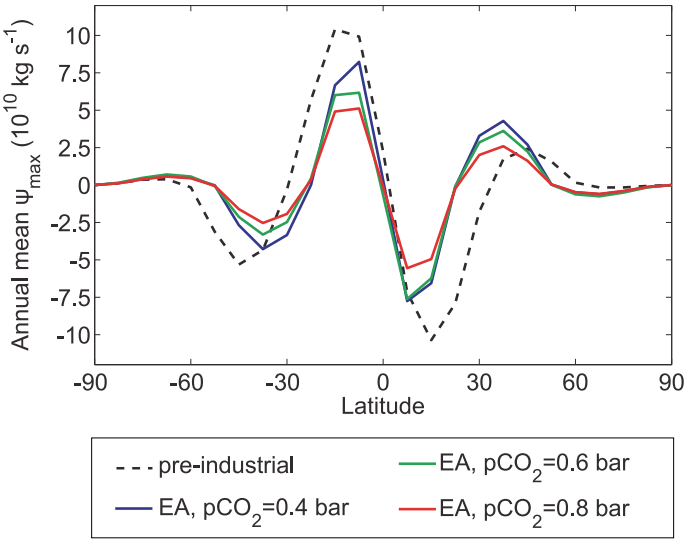

Fig. 11. Maxima of the atmospheric meridional stream functions for the pre-industrial state (black) and the three states of the early Archean (EA).

CPD
9, 525–582, 2013

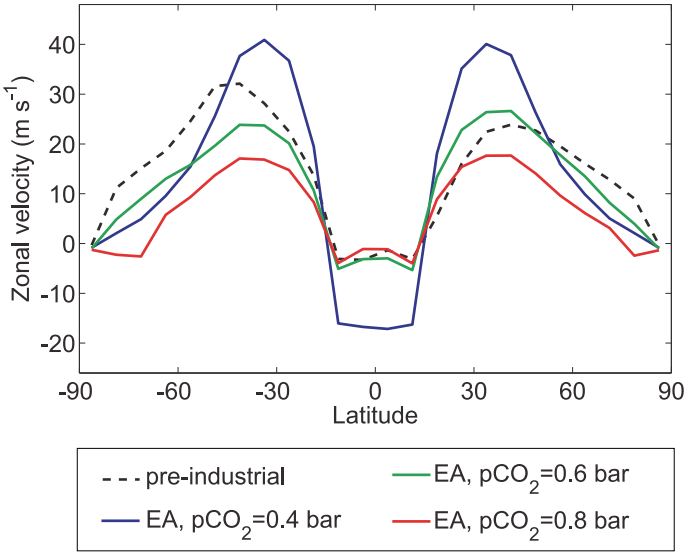

Fig. 12. Maxima of the annual mean zonal winds with respect to height for the pre-industrial state (black) and the three states of the early Archean (EA).

CPD
9, 525–582, 2013

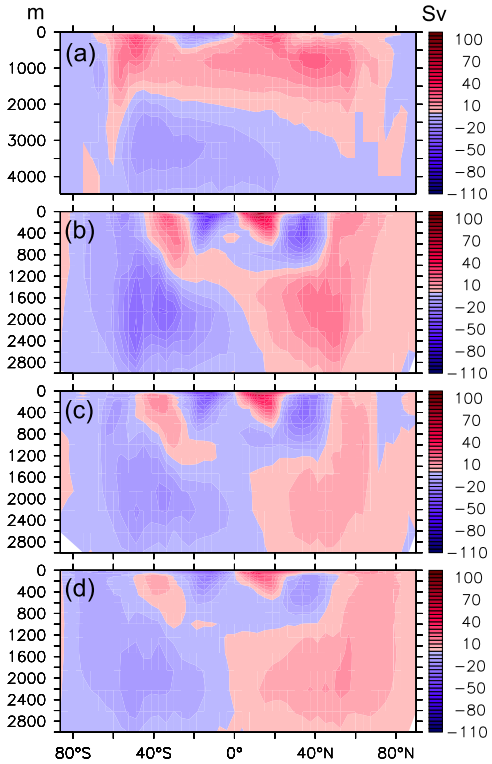

Fig. 13. Oceanic overturning stream functions for **(a)** the pre-industrial climate state and the three early Archean states (CO_2 partial pressure of 0.4, 0.6 and 0.8 bar in panel **(b)**, **(c)** and **(d)** respectively).

CPD
9, 525–582, 2013

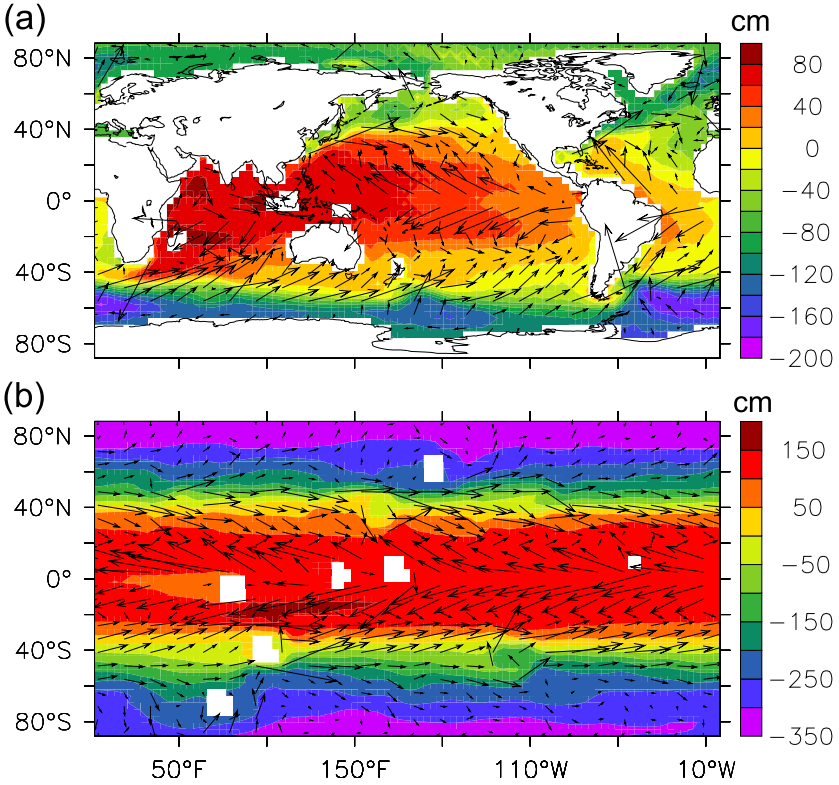

Fig. 14. Oceanic surface velocities (arrows) on top of sea-surface height anomalies (colour shading) for **(a)** the pre-industrial climate state and **(b)** the ice-free early Archean ($pCO_2 = 0.8$ bar).

CPD
9, 525–582, 2013

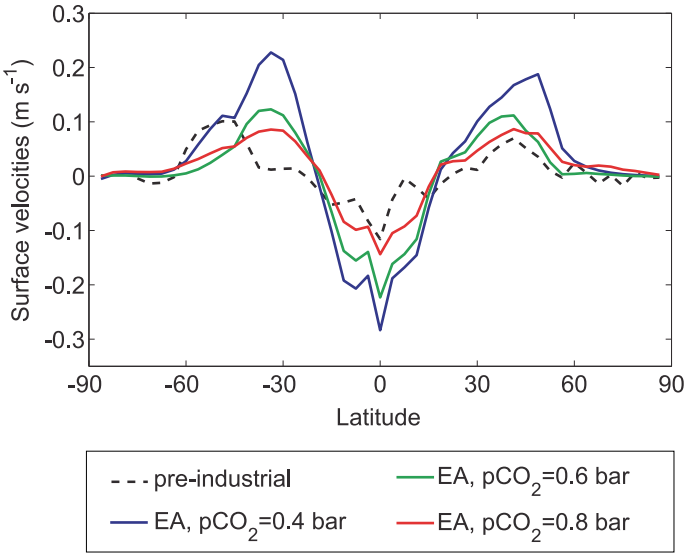

Fig. 15. Oceanic surface velocities (annual and zonal mean) for the pre-industrial climate state as well as the three climate states of the early Archean.

CPD
9, 525–582, 2013

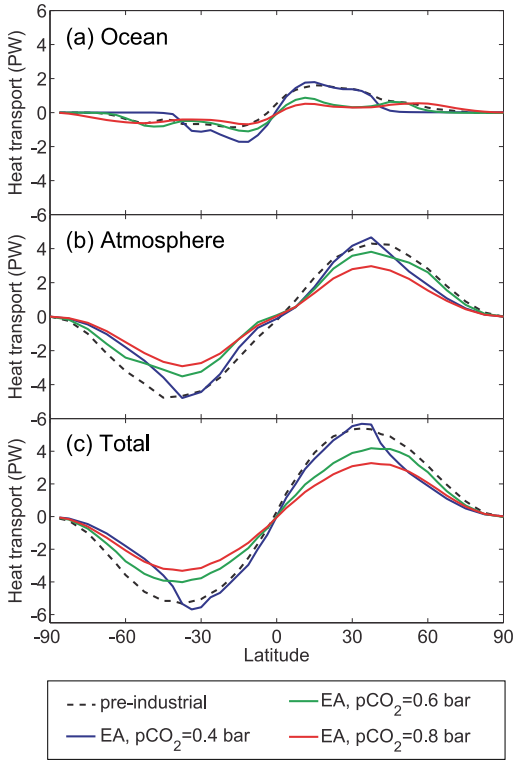

Fig. 16. (a) Oceanic, **(b)** atmospheric and **(c)** total meridional heat transport for pre-industrial conditions as well as for the three states of the early Archean (EA).

CPD
9, 525–582, 2013

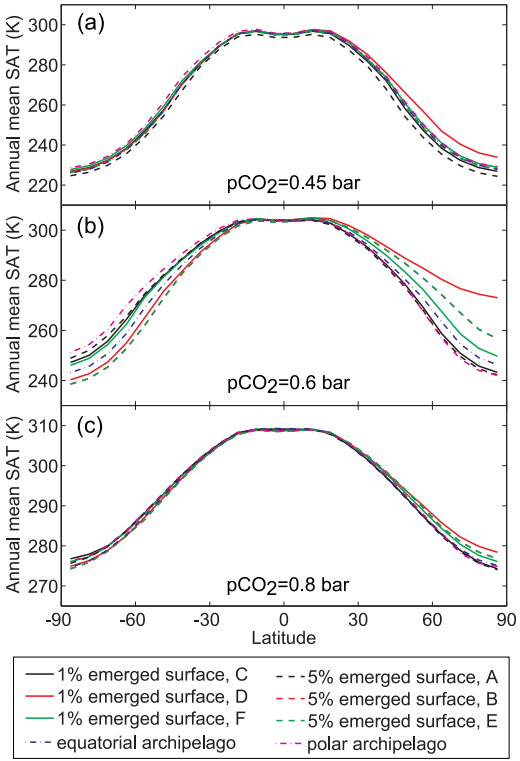

Fig. 17. SAT profiles corresponding to the set of 7 different early Archean topographies for **(a)** pCO_2 = 0.45 bar, **(b)** pCO_2 = 0.60 bar and **(c)** pCO_2 = 0.80 bar.

CPD
9, 525–582, 2013

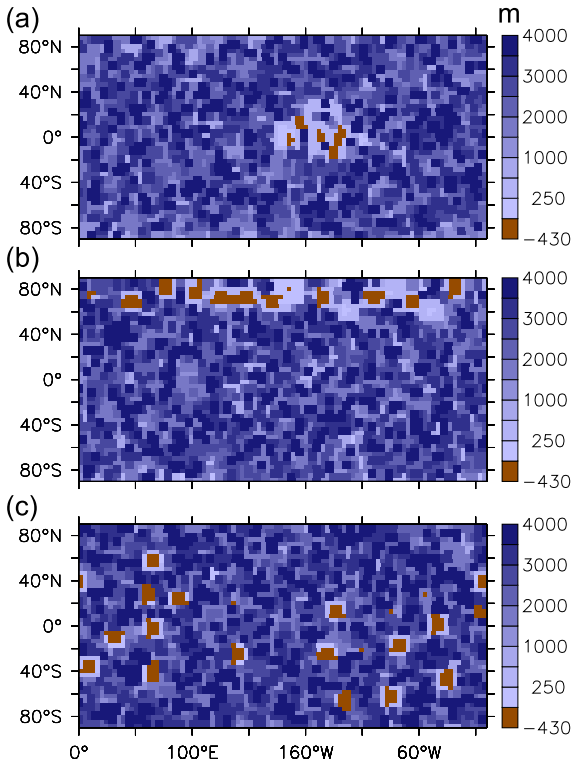

Fig. 18. Three exemplary topographies used in the uncertainty study: **(a)** equatorial archipelago, **(b)** polar archipelago and **(c)** a random topography with 5 % instead of 1 % emerged surface area.

CPD
9, 525–582, 2013

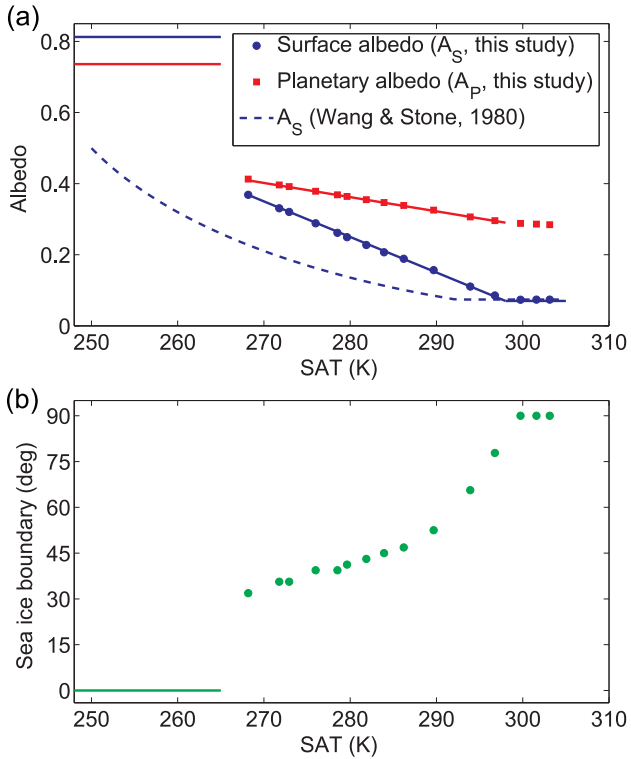

Fig. 19. Dependency of **(a)** surface and planetary albedo as well as **(b)** sea-ice boundary (mean of Northern and Southern Hemisphere values) on global mean SAT. The linear fits in panel **(a)** correspond to Eqs. (5) and (6). The constant albedo values for extremely low temperatures originate from a simulated snowball state. The dashed blue line in panel **(a)** shows the temperature dependence of the global mean surface albedo for present-day conditions according to Wang and Stone (1980) under the assumption of our snow and ocean albedo values.

CPD
9, 525–582, 2013